

Application of molybdenum trioxide in polymer
light-emitting diodes

Yong-Sig Shin

MPhil Thesis

University College London

June, 2012

Acknowledgments

Firstly, I would like to express my sincere gratitude to my supervisor Prof Franco Cacialli for all the valuable advice, support and guidance he has given me during every stages of my research. I am thankful to him for the opportunity he has given me at the group, where I have learned so much. I also thank my second supervisor Claire Carmalt for the initial support and guidance she provided me with, which allowed me to settle down as a research student.

Special thanks to Dr Oliver Fenwick and Dr Gustaf Winroth for training me at the early stages of my research on using the AFM, thermal evaporator and many other research tools in the lab, as well as showing me valuable research skills through excellent examples and discussions. Many thanks to Prof Apollo Mian for the time he spent helping me in the lab, as well as many discussions which aided in my research. Also thanks to Dr Sergio Brovelli for showing me how to use various tools in the lab.

Many thanks to all the group members; Francesco Di Stasio, Penglei Li, Dr Matia Lazzerini, Marten Tolk and Charlotte Flechon for making a bright and friendly atmosphere at the office. It was a pleasure to work in such positive environment. Finally I thank all the collaborators that visited the group, who also contributed to the warm atmosphere that the group always maintained.

Yong-Sig Shin June, 2012

Declaration

I certify that the work presented in this thesis is, to the best of my knowledge and belief, original, except as acknowledged in the text, and that the material has not been submitted, either in whole or in part, for a degree at this or any other university.

I acknowledge that I have read and understood the University's rules, requirements, procedures and policy relating to my higher research award and to my thesis. I certify that I have complied with the rules, requirements, procedures and policy of the University (as they may be from time time).

Name:

Signature:

Date:

Abstract

The thesis investigates the application of molybdenum trioxide (MoO_{3-x}) as hole injection layers (HILs) in polymeric light-emitting-diodes (PLEDs). Recent application of metal oxides into the PLED architecture has been motivated by the benefits of enhanced device performances, as well as, for the protection against the intrusion of oxygen and water into PLEDs. In this thesis, the performance of MoO_{3-x} HILs in PLEDs is investigated by fabricating ITO/ MoO_{3-x} /TFB/F8BT/Ca/Al electroluminescent devices and characterising their efficiency and luminescence properties. Also the performance of the device is studied within the context of the physical properties of MoO_{3-x} films and electroluminescent polymers, experimentally determined by various techniques. Three different types of PLEDs are fabricated and characterised, each incorporating MoO_{3-x} HILs with different electronic properties. Such difference in the films are achieved by post-deposition annealing of MoO_{3-x} films in air and nitrogen. It is determined that annealing MoO_{3-x} films in air has the effect of increasing their hole concentration. This improves the performance of MoO_{3-x} as hole injection layers in PLEDs. Upon annealing the as-deposited MoO_{3-x} HILs in air, the maximum current efficiency of PLEDs increases from 1.27 cd/A to 1.44 cd/A. Also the maximum luminescence increases from 2723 cd/m² to 5680 cd/m². Kelvin probe and electroabsorption spectroscopy measurements show that annealing MoO_{3-x} films has the effect of decreasing their work function by 0.3 eV. Finally, using time-correlated single photon counting (TCSPC), the photoluminescence (PL) lifetime of F8BT and TFB single layers, and TFB/F8BT bilayers are determined, with and without the presence of a MoO_{3-x} contact. The PL lifetime of excitons in pure F8BT is measured to decrease from 1300 to 760 ps upon incorporation of a MoO_{3-x} contact. In contrast to F8BT, the PL lifetime of TFB is determined to be 500 ± 40 ps, regardless of the presence of a neighbouring contact. The TFB/F8BT bilayers exhibit biexponential decay characteristics with two lifetime values; 800 ± 50 ps and 5000 ± 400 ps.

Contents

1	Introduction	6
1.1	π -conjugated semiconducting polymers	7
1.2	Charge carriers in conjugated polymers	8
1.3	Photophysics of conjugated polymers	10
1.4	Polymer light-emitting diodes	11
1.5	Injection and transport in PLEDs	14
1.6	Energy levels of diodes and metal/polymer interface	17
1.7	Application of metal oxides in PLEDs	21
1.8	Outline of thesis	22
2	Principal experimental techniques	24
2.1	Electroabsorption spectroscopy	25
2.1.1	Introduction to electroabsorption spectroscopy	25
2.1.2	Theoretical overview of electroabsorption	26
2.1.3	Measurement of the EA signal in conjugated polymers	30
2.1.4	EA in PLEDs as a probe for internal fields	32
2.1.5	The electroabsorption system setup	33
2.2	Fluorescence spectroscopy	35
2.2.1	Lifetime measurements in fluorescence spectroscopy	35
2.2.2	Time-correlated single photon counting	37
2.3	Macroscopic kelvin probe	39

<i>CONTENTS</i>	5
3 Dynamics of excitons at MoO_{3-x}/F8BT and MoO_{3-x}/TFB interfaces	42
3.1 Introduction	43
3.2 Experimental	45
3.3 Results	46
3.4 Discussions	50
3.4.1 Exciton quenching at MoO _{3-x} /F8BT interfaces	50
3.4.2 MoO _{3-x} /TFB interfaces and Exciplex	56
3.5 Conclusion	58
4 Molybdenum trioxide hole injection layers in polymer light-emitting diodes	59
4.1 Introduction	60
4.2 Experimental	61
4.3 Optical and electronic properties of annealed MoO _{3-x} films	63
4.4 Surface morphology of annealed MoO _{3-x} films	66
4.5 Work function decrease upon annealing MoO _{3-x} films	67
4.6 Current-Light-Voltage characteristics of PLEDs	72
4.7 Conclusion	74
5 Conclusion and outlook	75
5.1 Summary of the findings	76
5.2 Application of ITO/MoO _{3-x} /TFB as anodes in electroluminescent devices	77
5.3 Suggestions for future work	79
6 Bibliography	82

Chapter 1

Introduction

Polymer light-emitting diodes (PLEDs) are emerging as a technology the behind next generation of electronic displays and lighting systems due to their unique properties such as efficient and bright electroluminescence, flexibility, and ease of processing over large areas. A large body of on-going scientific research deals with the wide range of technological issues regarding the implementation of PLEDs into real world applications. It is of paramount importance to understand the science behind the operation of PLEDs in order to make significant technological leaps. This chapter presents a brief overview of the basic theory behind the properties of charge carriers and photophysics in conjugated polymers. Also the principles of physics governing the operation of PLEDs are reviewed, specifically focusing on the charge injection, transport properties and energy levels of PLEDs. The final section presents a brief summary of the recent application of metal oxides in PLEDs and a short outline of the thesis.

1.1 π -conjugated semiconducting polymers

Semiconducting conjugated polymers are long-chain carbon-based molecules, with extended π -orbitals. These polymers are considered promising materials for application in (opto)electronic devices due to their unique mechanical and optical properties, and potential low-cost manufacturing.^[1–6]

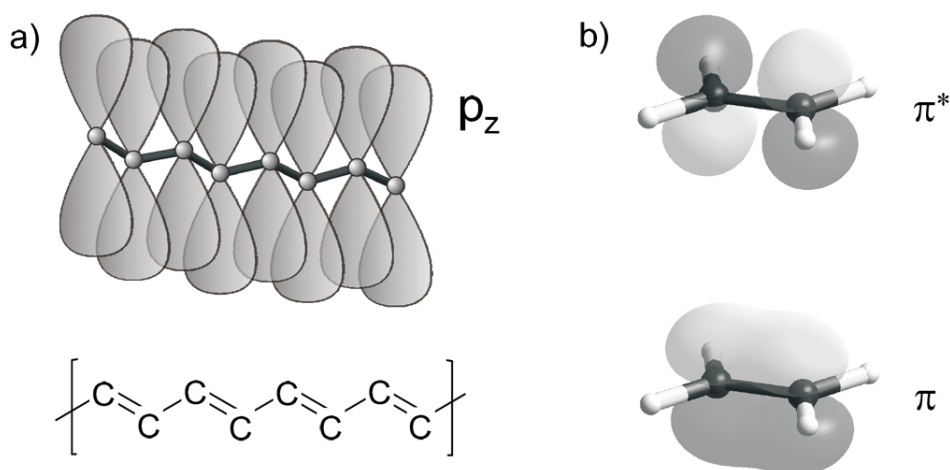


Figure 1.1: a) Schematic representation of p_z orbitals overlap in a conjugated segment of the polymer. b) Bonding π and antibonding π^* orbitals of the primary conjugated molecule; ethylene.^[7]

In general, semiconducting polymers have an alternating sequence of single and double bonds along the polymer backbones as illustrated in Figure 1.1 a). The valence electrons of carbon atoms in this sequence are arranged into three hybridised sp^2 orbitals, which leaves one p_z orbital perpendicular to the chemical direction, unhybridised. The sp^2 orbitals form strong σ bonds along the axis connecting adjacent carbon nuclei and provide the strong interatomic bonding, an important factor in determining the geometric structure of the molecule. The overlap of the p_z orbitals, perpendicular to the plane of the σ bonds gives rise to π bonds and to the formation of a π -electron cloud, delocalised over the conjugation length of the polymer. The unique semiconducting characteristics of conjugated polymers are due to the presence of filled bonding π -orbitals and unoccupied antibonding π^* -orbitals as shown

in Figure 1.1 b).

Semiconducting polymers are not ideal conjugated systems, they have breaks in the conjugation length due to twists and kinks, as well as due to chemical defects. This results in variations in the conjugation length of the segments and concomitantly in spread of the electronic energy levels, as illustrated in Figure 1.2. Hence, polymeric semiconductors cannot be described by delocalised valence and conduction bands formed by π and π^* orbitals, respectively. The π - π^* gap is defined as the energy separation between highest occupied molecular orbital (HOMO) and the lowest unoccupied molecular orbital (LUMO), where the spreads in energy levels of HOMO and LUMO are approximated by a Gaussian distribution of the density of states. The discrete π - π^* levels form quasi-continuous bands broadened by the interactions with neighbouring π orbitals. The ultimate width of polymer bands depends on the effective conjugation length of the polymer chains and is the cause of the decrease in the energy gap with conjugation length. Disorder contributes to the broadening of the energy levels and, alongside the vibrational and rotational energy levels, gives rise to the broad spectral features typically observed in the optical absorption and emission spectra of molecular solids. Most semiconducting polymers have an energy gap that lies in the range of 1.5 - 3 eV, which makes them ideal for applications in optoelectronic devices operating in the visible light range.

1.2 Charge carriers in conjugated polymers

Conduction in conjugated polymers occur when extra charges are added to the polymer chain. This is usually done by doping the polymer chain with electron acceptors or donors, or, in device configurations, by injecting charge from an electrical contact. As shown in Figure 1.3, when a charge is added to a polymer chain, the polymer relaxes to a new bonding geometry. For example, when an extra electron is put into a p_z orbital of poly(p-phenylenevinylene) (PPV) to form a lone pair, it disrupts the double bonding scheme. The structure relaxes by swapping the position of the carbon-carbon double and single bonds, giving rise to a chain that is an admixture

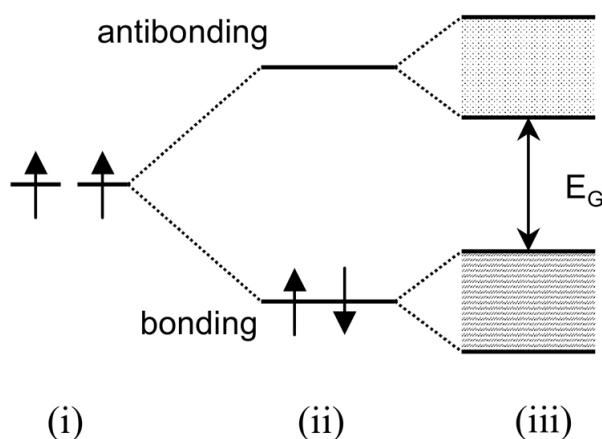


Figure 1.2: Schematic energy diagram showing the formation of band-like electronic states. i) atomic states; ii) bonding and antibonding states; iii) in a collection of atoms, interactions between orbitals broaden the bonding and antibonding states into quasi-continuous energy bands.^[8]

of the lower-energy benzoid and the higher energy quinoid PPV configurations. The structurally relaxed negatively charge state is called an electron polaron. Similarly, removal of an electron leads to a hole polaron. Further addition or removal of electrons can lead to doubly charged excitations called bipolarons. The formation of polarons or bipolarons creates new electronic states in the band gap, symmetrically located above the HOMO and below the LUMO.

Polaron states are responsible for electronic conduction in conjugated polymers. In the solid state, the polymer material is an amorphous matrix of a multitude of polymer chains with different conjugation lengths. Charge carriers in such disordered systems are localised in distorted lattice sites which leads to finite mean free path. Therefore transport in conjugated polymers occurs via a hopping mechanism^[10–13] through a manifold of localised molecular states. Polarons require a specific activation energy to escape the potential of their localisation sites for charge transport to occur. The variation in the conjugation length of the polymer segments, the presence of defects and of other topological and chemical disorder results in localisation sites with a spread of energy levels. Hopping through these localised polaronic states results in dispersive charge transport^[14] and carrier mobilities that are strongly electric field dependent and relatively small (e.g. Meyer *et al.*^[15] have

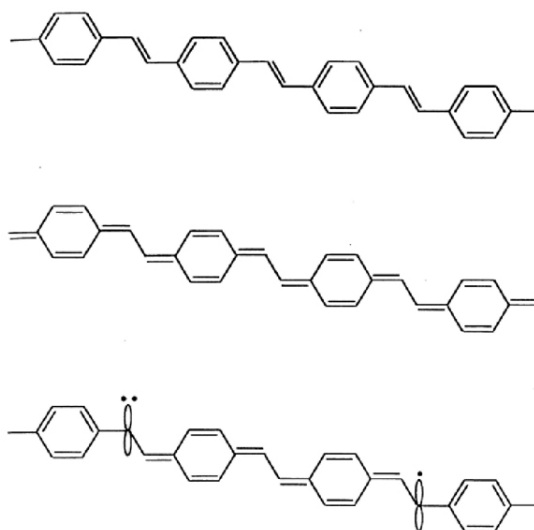


Figure 1.3: Schematic representation of the benzoid (top), quinoid (middle) and electron polaron (bottom) bond configurations in poly(p-phenylenevinylene). Adding an extra electron modifies the lower energy benzoid bond scheme to form a lone pair (bottom left). Also switching from the higher energy quinoid configuration back to the benzoid configuration results in formation of an unpaired p_z orbital (bottom right).^[9]

determined the hole mobility of PPV to be $\mu \sim 10^{-8} \text{ m}^2/\text{Vs}$ at room temperature).

1.3 Photophysics of conjugated polymers

A photon is emitted in a conjugated polymer via radiative recombination of a polaron-exciton, which consists of two Coulombically bound polarons of opposite charge. The wavelength of the emitted photon is determined by the energy separation between HOMO and LUMO. The inverse process to light emission is absorption, where a polaron is excited upon absorbing an incident photon. The large Stokes' shift separating the peaks of the emission and absorption spectra is due to the localisation of the polaronic states and their strong interaction with the chain. The dielectric constant of the order of 3 as compared to 10 in inorganic semiconductors results in strongly bound Frenkel-like localised excitons. Hence, exciton effects are important at room temperature in contrast to inorganic Wannier type excitons with a binding energy of about kT at room temperature. Excitons in conjugated polymer do not readily undergo thermal dissociation, giving rise to important spectral

features in the spectroscopy even at room temperature.

In the emission process, a neutral polaron exciton is formed when two polarons of opposite charge recombine prior to radiative decay, where the lattice relaxes by local structural modification. The amplitude of Stokes' shift is determined by the magnitude of lattice relaxation. Emission is from the radiative decay of a bound polaron exciton with a binding energy of a few tenths of an electron volt,^[16,17] The large binding energy is a consequence of the electron-electron interaction which provide Coulomb attraction between the electron and the hole as well as simultaneously acting to lower the polaron-exciton lattice relaxation with respect to separated polarons.

The appearance of an apparent Stokes' shift can be due to a combination of several factors. Emission takes place from an electronic state that is different from the one involved in the absorption process. This is the case for instance when there is crossing from a high energy state to a lower triplet state, or, energy transfer from a high to a low energy state. Such intersystem crossing may inhibit the fluorescence since the excitation relaxes to a metastable electronic state that is poorly coupled to the ground state; non-radiative decay can dominate and the luminescence is quenched. Disorder leads to localisation of the wavefunctions and a distribution of effective conjugation lengths. Absorption can take place from anywhere in the sample and is then characterised by inhomogeneous broadening. The excited electron-hole pairs, whether bound or not, can subsequently travel along and among chains via a random walk process and can be trapped on those chain segments with the longest conjugation length (lowest energy), from which emission then occurs. In such a case, not only is the emission peak red-shifted with respect to the absorption peak but the emission bands appear much sharper than the absorption bands.

1.4 Polymer light-emitting diodes

After the discovery of electroluminescence in conjugated polymers in 1989, the first polymer light-emitting diode (PLEDs) was reported by Burroughes^[1] that year.

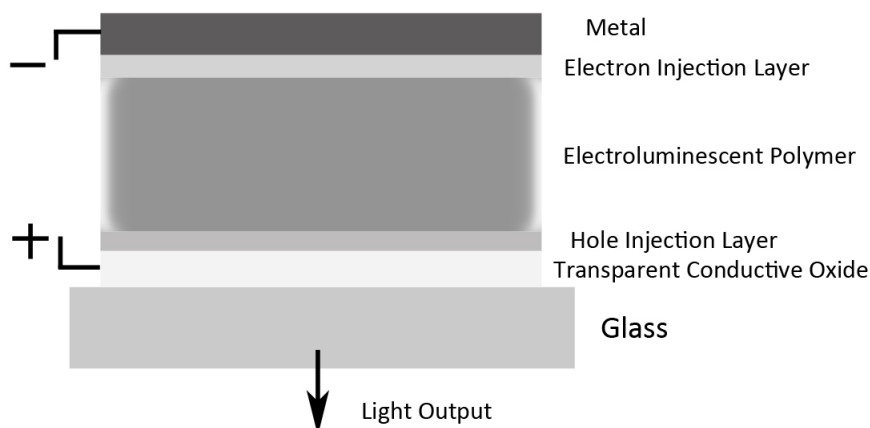


Figure 1.4: Schematic representation of polymer light-emitting diodes

Research and development in the use of conjugated polymers as the active semiconductor in PLEDs have advanced rapidly and are seen to be promising due to their efficient light generation, mechanical flexibility and low-cost manufacturing capability using solution processing. Understanding the physical processes that control the properties of these devices is vital to the development process.

A typical device (Figure 1.4) is prepared by spin-coating a conjugated polymer on top of a high work-function transparent electrode, usually indium tin oxide (ITO), which acts as a hole injecting contact. Subsequently, a top metal electrode (cathode) is applied as an electron-injecting contact, employing low work function metal such as calcium. Finally a layer of Al is deposited on top of the cathode for protection against oxygen. As shown in Figure 1.5, there are three main processes governing the PLED performance upon application of an external electric field: (a) charge injection, (b) charge transport and (c) exciton recombination. A forward bias is applied across the two electrodes, where the resulting electric field drives a bipolar current through the polymer film. Holes from anode and electrons from cathode are transported towards each other in the applied field with subsequent formation of excitons under their mutual electron-hole Coulomb attraction. Light is emitted upon exciton recombination, where the emission wavelength can be tuned, depending on the chemical structure and composition of the active layer.

Usually, the efficiency of a PLED is estimated by the internal quantum efficiency,

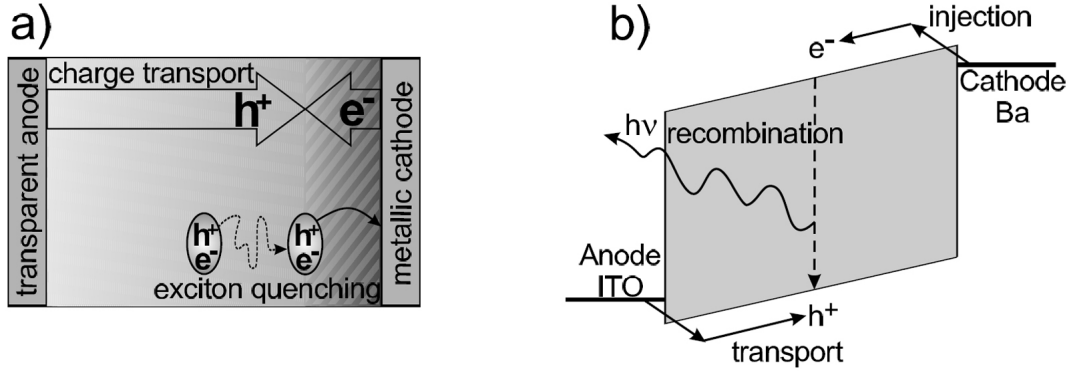


Figure 1.5: a) The PLED architecture is shown together with a simplified representation of the processes of the charge transport and the exciton quenching at the cathode. b) Schematic energy level diagram for ITO/polymer/Ba LED. ^[7]

defined as the ratio of the number of photons produced within the device to the number of electrons flowing in the external circuit; ^[18]

$$\eta = \gamma r_{st} q \quad (1.1)$$

where γ is the ratio of the number of exciton formation events within the device to the number of electrons flowing in the external circuit, r_{st} is the fraction of excitons formed as singlets and q is the efficiency of radiative decay of these singlet excitons. The external quantum efficiency accounts only for the photons that escape the device;

$$\eta = \gamma r_{st} q \eta_c \quad (1.2)$$

where η_c represents the proportion of photons produced that escape the device. Generally, the electrical excitation of the polymer is expected to produce excitons with spin wavefunctions in the triplet and singlet configurations in the ratio 3:1, although recently singlet exciton formation ratio higher than 25 % in organic compounds with an extended conjugated system has been suggested. ^[19] Radiative decay from triplets is spin-forbidden and often very inefficient and 60 - 75 % of electron-hole pairs are lost as triplet states. Also, additionally to the intrinsic non-radiative exciton quenching in conjugated polymer films, there are radiative and non-radiative

rates that are modified by the metallic electrodes. Hence, many of the technological and scientific challenges revolve around maximising the emission efficiency. This involves achieving effective charge injection, a good balance of electron and hole currents, maximising the probability of exciton formation and minimising non-radiative recombination.^[6] One of the most effective strategies to improve the emission efficiency has been the application of multi-layer devices,^[2,20] allowing one to minimise charge injection barrier from the electrodes to the electroluminescent polymer layers. It also allows one to move the recombination zone away from the electrode that injects the low mobility carrier and prevents the majority carriers travelling through the device without recombining.^[21]

1.5 Injection and transport in PLEDs

Charge injection is a vital process that must be controlled for efficient performance of PLEDs. Prior to entering the polymer layer, charges have to overcome (Schottky) injection barriers that are determined by the offsets between the electrode work functions and HOMO and LUMO of the polymer, respectively. Excess of one type of charge carriers may be present in the polymer layer due to unbalanced injection of holes and electrons, resulting in low conversion efficiency. Mobility of charge carriers ($\mu \sim 10^{-8} \text{ m}^2/\text{Vs}$) in conjugated polymers is typically 5 - 10 orders of magnitude lower than in inorganic semiconductors due to a high degree of energetic and structural disorder. Also it has been observed that the electron conduction is significantly smaller than the hole conduction due to the presence of electron traps^[22] or to a lower electron mobility.^[23] Compared to inorganic systems, Schottky barriers in undoped conjugated polymers are found to vary more strongly upon the electronic characteristics of the injecting contact.^[24-27] Therefore charge injection processes in PLEDs depend largely upon the electrode material.

Two charge injection mechanisms^[28] based on established inorganic semiconductor device physics, have been employed to describe the dependence of the current on the barrier height, electric field and temperature: (a) Fowler-Nordheim quantum

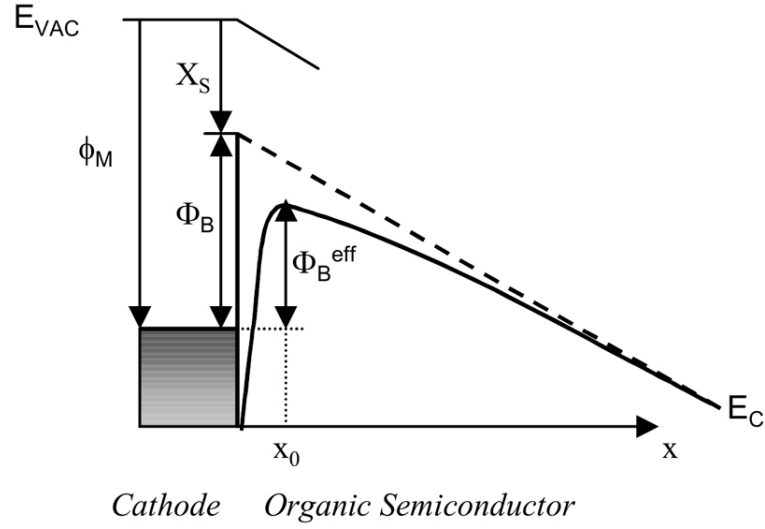


Figure 1.6: Schematic energy diagram of the metal-semiconductor contact. E_{vac} is the vacuum level, ϕ_m is the work function of the metal, Φ_B is the barrier height at zero electric field, x_0 is the distance from the metal at which the barrier is maximum, and χ_s is the electron affinity of the semiconductor. The solid line is the semiconductor conduction band minimum, E_c . The effective barrier height Φ_B^{eff} is field dependent and is determined by the sum of the applied field and the image force.^[8]

mechanical tunneling and (b) thermionic emission. The Fowler-Nordheim tunneling predicts;^[27]

$$I \propto F^2 \exp\left(\frac{-\kappa\phi_B^{3/2}}{F}\right) \quad (1.3)$$

where I is the current, F is the electric field, ϕ_B is the the barrier height at zero electric field and κ is a constant in terms of the carrier effective mass. Thermionic emission over the metal/semiconductor interface predicts a current of;^[28,29]

$$I = A^* T^2 \exp\left(\frac{-\phi_B^{eff}}{kT}\right) \quad (1.4)$$

where A^* is known as the effective Richardson constant and ϕ_B^{eff} is the effective barrier height which accounts for the field dependence. Schematic energy diagram of the metal-semiconductor contact is illustrated in Figure 1.6. It should be noted that neither Equation 1.3 or 1.4 are able to provide an accurate quantitative account for the observed experimental current-voltage characteristics.

Charge carriers are injected from the Fermi level of the metal electrode into a

polaron level near the metal/semiconductor interface by means of the two injection mechanisms mentioned above. Unlike crystalline semiconductors where charge transport occurs via long range propagation in extended states, in conjugated polymers it occurs through polaron hopping between localised states.^[30-32] The majority of charge carriers are injected into the conjugated polymer at the metal contact given that the carriers have overcome the random barriers present at the interface.^[31] At low electric field, it is less likely for the carriers to overcome these barriers and end up recombining at the metallic interface. The probability of carriers overcoming the barriers increase with the applied electric field where electrons and holes subsequently drift towards the anode and cathode, respectively, in the bulk of the polymer film.

Two limiting regimes for the current are known to exist for devices where the predominant charge carriers are either electrons or holes. In the case where large energy barriers or large mobilities are present in the device, the current is limited by the rate of carrier injection from the electrode into conjugated polymers and the current is strongly dependent on the height of the injection barrier. For low energy barriers or low mobilities, the current in the device is space-charge limited (SCL). In this case, the charge transport away from the contact occurs at a slower rate than injection. The limit to the current in the device is set by the modification of the local electric field caused by the accumulation of space charge near the contact.

Marcus' established theory of electron-transfer processes for biological and chemical reactions can be applied to describe the charge transport of polaronic carriers in conjugated polymers, given that the temperature is sufficiently high.^[33] In order for the localised polaron to hop from their initial to final molecular site, both sites must be equally distorted to a common configuration. This leads to thermally activated transport even in the absence of disorder. In the non-adiabatic limit, where the timescale for electron hopping is longer than that of the lattice vibrations, the mobility is given by;^[34,35]

$$\mu = \frac{ea^2}{k_B T} \nu \exp\left(\frac{-E_p}{2k_B T}\right) \quad (1.5)$$

where e is the the electronic charge, a is the typical hopping distance, k_B is Boltzmann's constant, T is temperature, E_p is the activation energy required for hopping and ν is the attempt frequency;

$$\nu = \frac{\sqrt{\pi}J^2}{\hbar\sqrt{2E_p k_B T}} \quad (1.6)$$

where J is the nearest-neighbour interaction energy and \hbar is Plank's constant. It should be noted that, in most experimental systems the detectable polaronic character of the charge carriers are modified by the effects of disorder.^[36] In any solution-deposited thin film, disorder causes the energy of a polaronic charge carrier on a particular site to vary across the polymer network, resulting in significant broadening of the electronic density of states.

1.6 Energy levels of diodes and metal/polymer interface

The mechanisms of energy level alignment in diodes must be understood well in order to produce efficient devices since it dictates the magnitude of Schottky barrier height and therefore the injection properties of diodes. It is difficult to interpret the experimental data solely based on the alignment mechanisms and also to fabricate an ideal and reproducible interface. Since the metal-semiconductor interface can be a complex quasi-2D system with unknown atomic geometry, interdiffusion, transfer of charge, defect states and new chemical compound formation, that can all modify the electronic alignment at the interface. However there are general theoretical models and conditioned experiments that can predict energy alignment in diodes, with a precision in the tenth of an eV range. This section deals with three theoretical models that predict how the electronic bands of semiconductors and metals align after contact: (a) Schottky, (b) Bardeen and (c) Tersoff's Charge Neutrality Level theories. Figure 1.7 shows an energy band diagram of metal-semiconductor contact according to the Schottky and Bardeen model.

The Schottky model approximates the barrier height for electrons without con-

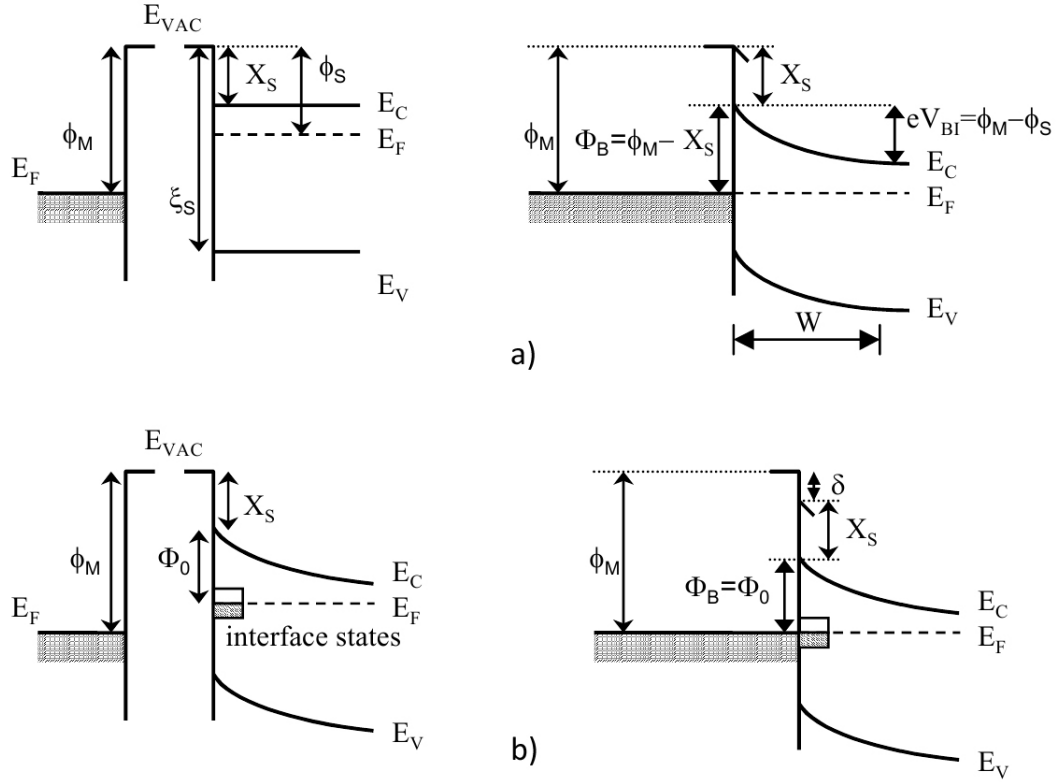


Figure 1.7: Energy band diagram of metal-semiconductor (n -type) contacts, before and after formation (left and right diagrams, respectively); a) accounted by the Schottky model and b) accounted by the Bardeen's model.^[8]

sidering the dipole layers and charged states at the interface and is given by;^[37,38]

$$\Phi_B(e^-) = \phi_M - \chi_s \quad (1.7)$$

where χ_s is the electron affinity of the semiconductor and ϕ_M is the work function of the metal. The barrier height for holes is determined by the difference between the ionisation potential of the semiconductor ζ_s and ϕ_M ;^[39,40]

$$\Phi_B(h^+) = \zeta_s - \phi_M \quad (1.8)$$

The Schottky model neglects charge transfer and surface reconstruction occurring at the interface, which may introduce an interfacial dipole layer. This causes a discontinuity in the electrostatic potential at the interface.

Bardeen's model accounts for the role of dipoles and charged states at the metal-semiconductor interface by the proposition that the metal's Fermi level is 'pinned' by a high density of localised states present on the semiconductor surface.^[38,41] Given that the density is high enough, all the charge from the metal can be transferred to these localised states without significantly modifying the Fermi level of the metal. This process of charge transfer at the interface creates a dipole layer that effectively aligns the Fermi level of the metal to that of the surface states in the semiconductor. Consequently, the barrier height is independent of the metal's work function upon metal-semiconductor contact.

Tersoff's charge neutrality level (CNL) model studies the nature of the Fermi level pinning in further detail.^[38,42,43] A dipole layer at the metal-semiconductor interface is formed as a consequence of interface states present in the forbidden energy gap of the semiconductor. For a simple case of a metal-metal junction, electrons flow from one metal with the lower work function to the other with the higher work function. Transfer of charge creates a dipole layer, which aligns the two Fermi levels. At equilibrium, the magnitude of the dipole is equal to the mismatch between the work function of the metals. In the case of a metal-semiconductor junction, transfer of charge occurs due to the tails of the metallic wave function decreasing exponentially in the adjacent semiconductor gap states, given that the metal's work function lies between the valence band maximum and the conduction band minimum. The mismatch between the metal Fermi level and E_{cnl} of the semiconductor, denoted the charge neutrality level (analogous to the Fermi level of the metal) can be defined as;^[44]

$$E_F - E_{cnl} = S(E_{cnl} - \phi_M) \quad (1.9)$$

where $S = |d\Phi_M/d\phi_M|$ is a constant known as the interface parameter^[45,46] that measures the amount of pinning at the interface. Note that the mismatch is reduced by the newly formed dipole layer. A perfect alignment between the E_{cnl} of the semiconductor and the Fermi level of the metal is only possible for semiconductors with

a large optical dielectric constant, ϵ_∞ , or high density of interface states. Therefore E_{cnl} is an intrinsic property of the semiconductor and the Schottky barrier height of a particular semiconductor is independent of the metal and its work function. Based on above assumptions, Tersoff's CNL model predicts a metal-semiconductor barrier height of;^[47]

$$\Phi_B = S(\phi_M - \chi_s) + (1 - S)\Phi_0 \quad (1.10)$$

where Φ_0 represents the pinned value of the barrier for a specific semiconductor surface. The proportionality factor is a characteristic of each semiconductor and has limits of $S_{min} = 0$ and $S_{max} = 1$. Notice that with Equation 1.9, as S approaches to 1, a Schottky barrier height is observed and as S approaches to 0, a Bardeen barrier height is observed, independent of ϕ_M .

Generally in PLEDs, low work function electrodes make good electron injectors and high work function electrodes make good hole injectors. For metals whose work function lies inside the polymer π - π^* gap, the Schottky model can accurately describe the dependence of the barrier height upon the work function of the metal as expressed in Equations 1.7 and 1.8. The Schottky model is valid for conjugated polymer systems where their low concentration of surface states, semi-insulating properties and low dielectric constant, ϵ , results in a small dipole layer. However many factors can affect the interfacial electronic structure and line-up at the organic-semiconductor/metal junction.^[48,49] These factors include chemical reactions, diffusion at the interface and the presence of contaminants which also depend on the atmosphere in which the structures are fabricated and characterisations are carried out.^[50,51] Hence it is vital to maintain low levels of impurities in conjugated polymers during fabrication, as well as keeping ideal evaporation conditions in order to have reproducible results.

1.7 Application of metal oxides in PLEDs

Application of metal oxides in conjugated polymer based devices has received much attention in the past five years, mainly due to the benefits of air stability and enhanced performance to the devices.^[52] Despite promising expectations of technological impact, electronic devices based on conjugated polymers are not yet fully utilised in large scale commercial applications. Device instability is caused by vulnerability to the diffusion of oxygen and water vapour into the active layers.^[53–55] Most semi-conducting polymer materials degrade when exposed to humidity and/or oxygen. Heeger *et al.*,^[52] applied a 30 nm-thick titanium oxide (TiO_x) film as an electron injecting layer between the active layer and the aluminium cathode in PLEDs. It is suggested that TiO_x layer acts as a shielding and scavenging layer which prevents the intrusion of oxygen and humidity into the active polymers, thereby improving the lifetime of devices. Research of Fujishima and Honda^[56] suggests that TiO_x 's oxygen/water protection and scavenging effect originates from the combination of photocatalysis and inherent oxygen deficiency.^[57–59] Other metal oxides that has been incorporated into conjugated polymer based device architecture include zinc oxide (ZnO),^[60] cesium carbonate (Cs_2CO_3)^[61] and zirconium dioxide (ZrO_2)^[62] as electron injection layers, and, molybdenum oxide (MoO_{3-x})^[63] and tungsten oxide (WO_3)^[64] as hole injection layers.

As well as providing air stability, application of metal oxides as electron/hole injection layer has shown promising evidence of improving the performance of devices. In the case of application of titanium oxide as an electron transport layer, it also acts as a hole blocking layer at the interface of the cathode and the conjugated polymer layer,^[65] thereby improving the device efficiency. ZnO is another promising candidate as an electron injection layer due to its good electrical conductivity and low work function. Also the highly transparent property of most metal oxides make them an effective connecting structure for tandem LEDs. An example tandem LED configuration^[61] consists of a thin metal layer as the common electrode (5 nm of Al), MoO_{3-x} hole-injection layer on one side of the common electrode, and Cs_2CO_3

electron injection layer on the other side. There are a number of different deposition techniques that may be employed to produce metal oxide films, such as sol-gel, thermal evaporation and chemical vapour deposition techniques. Also metal oxides are mechanically and electrically robust as well as being low cost and environmentally stable. Finally metal oxides such as ZnO can be deposited in a large variety of nanostructures,^[66,67] where the controllability of the film morphology allows further enhancement to device performance.

1.8 Outline of thesis

This thesis investigates the application of molybdenum trioxide (MoO_{3-x}) as hole injection layers in ITO/ MoO_{3-x} /TFB/F8BT/Ca/Al (ITO : Indium tin oxide, TFB : poly((9, 9-dioctylfluorene)-alt-N-(4-butylphenyl)diphenylamine), F8BT : poly(9,9-dioctylfluorene-alt-benzothiadiazole, Ca : Calcium, Al : Aluminium) electroluminescent devices. This is achieved by fabricating various device configurations as well as their isolated material components and characterising them using a wide range of experimental techniques.

Chapter 2 presents the theoretical and experimental overview of the principal experimental techniques employed for the thesis. The review of electroabsorption (EA) spectroscopy as a tool to measure the internal fields of polymer light-emitting diodes (PLEDs) is presented, where the technique is used to measure the built-in voltage of PLEDs reviewed in Chapter 4. Also the principle of photoluminescence (PL) lifetime measurements using time-resolved fluorescence spectroscopy is presented, focussing on time-correlated single photon counting (TCSPC). The technique is used to measure the radiative lifetime of excitons in conjugated polymers studied in Chapter 3. Finally the mechanism of macroscopic Kelvin probe is described, where the technique is employed to measure the work function of MoO_{3-x} in Chapter 3, as a complementary data to the built-in voltage data measured by the EA spectroscopy.

Chapter 3 studies the dynamics of exciton quenching in conjugated polymers due to the presence of a MoO_{3-x} contact. The investigation is relevant to the devices

fabricated in Chapter 4 since MoO_{3-x} interlayers form an interface with the TFB layer. Using time-correlated single photon counting, the photoluminescence (PL) lifetime of F8BT and TFB singles layers, and, TFB/F8BT bilayers are determined, with and without the presence of a MoO_{3-x} contact. The study focuses on using the theory of Förster energy transfer at the interface of MoO_{3-x} and the conjugated polymer to explain the change in PL lifetimes of polymeric excitons brought on by MoO_{3-x} contacts. The energy transfer model represents the excitons in conjugated polymers as a oscillating dipole and the MoO_{3-x} contact as radiation absorbing mirror. The theory allows us to quantify the amount of exciton quenching brought on by the MoO_{3-x} contact.

Chapter 4 studies the effect of post-deposition annealing MoO_{3-x} hole injection layers (HILs) in PLEDs on their electronic state and work function properties. This is achieved by fabricating and characterising the performance of ITO/ MoO_{3-x} /TFB/F8B-T/Ca/Al electroluminescent devices using current-light-voltage (*JVL*) and EA measurements, and comparing the data with the absorption spectra and work function data of isolated MoO_{3-x} films. Three different types of MoO_{3-x} films are produced and applied as HILs in device configurations; achieved by post-deposition annealing thermally evaporated MoO_{3-x} films in air and nitrogen (the third type being as-deposited film). The study focuses on the modification of optical and electronic properties of MoO_{3-x} films brought on by post-deposition annealing, where this is supported by a wealth of literature available on the thermochromic properties of MoO_{3-x} . A change in electronic states of MoO_{3-x} films was found to have a large effect on their operation as hole injection layers in PLEDs.

Chapter 5 presents a brief summary of the findings in the thesis, as well as explaining the device performance presented in Chapter 4 in connection with the various properties of MoO_{3-x} and MoO_{3-x} /conjugated polymer interface found in Chapters 3 and 4. Finally future research on the application of MoO_{3-x} in PLEDs are suggested.

Chapter 2

Principal experimental techniques

This chapter presents the theoretical and experimental overview of the principal experimental techniques used for the characterisation of electroluminescent devices and their material components fabricated for the thesis. Firstly the theoretical study of the application of electroabsorption (EA) spectroscopy as a tool to measure the internal fields of polymer light-emitting diodes (PLEDs) is presented. The EA technique is used to measure the built-in voltage of PLEDs reviewed in chapter 4. Secondly the principle of photoluminescence lifetime measurements in time-resolved fluorescence spectroscopy is presented, focussing on time-correlated single photon counting (TCSPC). The technique is employed to measure the radiative lifetime of excitons in conjugated polymers studied in Chapter 3. Finally the working mechanism of macroscopic Kelvin probe is described, where the technique is used to measure the work function of MoO_{3-x} films.

2.1 Electroabsorption spectroscopy

2.1.1 Introduction to electroabsorption spectroscopy

Electroabsorption is a form of modulation spectroscopy^[68] that measures the normalised variation of the transmission of light through a sample upon application of a periodic electric field.^[69] Modulation spectroscopy is an optical technique that allows one to study the physics of semiconductor devices by the measurement and interpretation of changes in the optical spectra when modifying the measurement conditions. Electroabsorption spectroscopy is unique in that it allows to measure data from actual working devices without disrupting their physical state.

The transmitted intensity of the light through a sample for normal incidence can be written as;^[70,71]

$$I_T = I_0(1 - R)^2 e^{-\alpha d} \quad (2.1)$$

where I_0 is the incident intensity, R is the reflection coefficient, α is the absorption coefficient and d is the sample thickness. It is assumed that the reflection coefficient is the same at the front and back surfaces of the sample.

The absorption and reflection coefficients of the sample is modified by the application of an electric field. The field-induced changes of the transmitted intensity is given by;

$$\frac{\delta I_T}{\delta F} = -I_0 e^{-\alpha d} \left[d(1 - R)^2 \frac{\delta \alpha}{\delta F} + 2(1 - R) \frac{\delta R}{\delta F} \right] \quad (2.2)$$

Dividing Equation 2.2 by Equation 2.1 (the unperturbed intensity) gives;

$$\frac{\Delta T}{T} = \frac{\Delta I_T}{I_T} = -d\Delta\alpha + \frac{2}{1 - R}\Delta R \quad (2.3)$$

The second term of Equation 2.3 can be neglected for the typical operating conditions of electroabsorption experiments and therefore the equation can be rearranged to yield;^[70,71]

$$\frac{\Delta T}{T} \cong -d\Delta\alpha \quad (2.4)$$

Equation 2.4 shows that the field induced normalised variation in transmission is directly proportional to the field-induced variation in the absorption coefficient.

2.1.2 Theoretical overview of electroabsorption

A brief theoretical overview of electroabsorption is presented in this section where the origin of nonlinear optical phenomena in materials and the Stark effect in conjugated polymer is discussed.

Firstly the electroabsorption response is described in a semiclassical approach where the response is considered as a nonlinear optical phenomena.^[72-74] The interaction between electron in an atom and the electric field induces a force, qF , which displaces the centre of electron density away from the nucleus. The bulk polarisation, \vec{P} , representing the induced dipole in the material, opposes the externally applied field and is given by;

$$\vec{P} = \varepsilon_o \chi \vec{F} \quad (2.5)$$

where χ is the electric susceptibility tensor, \vec{F} is the electric field and ε_o is the dielectric constant of the vacuum.

The relationship between the electric susceptibility, χ , the dielectric constant, ε_r , and the (complex) index of refraction, N , is given by;

$$\varepsilon_r = (1 + \chi) = N^2 = (n + ik)^2 \quad (2.6)$$

where n is the refractive index and k is an attenuation factor, which is a measure of the loss in power of a wave propagating through the material and is proportional to the absorption coefficient, α . The proportionality relationship between α and k is given by;

$$\alpha = \frac{4\pi}{\lambda} k = \frac{2\pi}{n\lambda} \text{Im}(\varepsilon_r) \quad (2.7)$$

where λ is the wavelength of the light.

Given that the induced dipole moments of the material respond instantaneously to an applied electric field, the polarisation in a medium can be written as a power

series in the electric field;

$$P = \varepsilon_o(\chi^{(1)}F + \chi^{(2)}F^2 + \chi^{(3)}F^3 + \dots) \quad (2.8)$$

where $\chi^{(n)}$ is the n^{th} order susceptibility. For majority of materials, orders higher than $\chi^{(3)}$ are rare to observe^[74] and $\chi^{(2)}$ vanishes in media with inversion symmetry since the polarisation changes sign when the field is reversed. Hence, for centrosymmetric materials such as conjugated polymers, the polarisation can be defined as;

$$P = \varepsilon_o\chi_{eff}F = \varepsilon(\chi^{(1)} + \chi^{(3)}F^2)F \quad (2.9)$$

Therefore, the variation of χ_{eff} with the electric field is given by;^[75]

$$\Delta\chi_{eff} = \chi_{eff}(F) - \chi_{eff}(0) = \chi^{(3)}F^2 = 2N\Delta N = \Delta\varepsilon_r \quad (2.10)$$

Equation 2.10 allows the calculation of the third order nonlinear susceptibility for isotropic materials, which is given by;

$$\chi^{(3)} = \frac{2N\Delta N}{F^2} \quad (2.11)$$

The variation in the imaginary part of the complex refractive index is $\text{Im}(\Delta N) = \Delta k$, where Δk can be extracted from the electroabsorption response;

$$-\frac{1}{d} \frac{\Delta T}{T} \cong \Delta\varepsilon = \frac{4\pi}{\lambda} \Delta k \quad (2.12)$$

Finally, the third order nonlinear susceptibility $\chi^{(3)}$ in Equation 2.11 can be derived from a Kramers-Kroenig analysis of the absorption and electroabsorption spectra of the conjugated polymer film.

The mechanism of the field-induced variation of electroabsorption response has also been investigated via a quantum mechanical approach. The change in the absorption coefficient, ε , with the electric field for conjugated polymers can be de-

scribed by the model of Stark shift of the molecular energy levels. The model assumes that the electronic states of conjugated polymers are localised to a high degree.

The Hamiltonian of the unperturbed molecular electronic state $|\psi_j\rangle$ is modified under the presence of an electric field by the addition of the following perturbation;^[76]

$$H' = e\mathbf{F} \cdot \mathbf{r} = eFz \quad (2.13)$$

where $-e$ is the charge of the electron and the electric field is directed along the z direction. The energy of state $|\psi_j\rangle$ is corrected to the first order which is defined as $\langle \text{bra} || \text{ket} \rangle$ of the state over the operator H' and is given by;

$$\Delta E_j^{(1)} = eF\langle \psi_j | z | \psi_j \rangle \quad (2.14)$$

Equation 2.14 is known as the linear Stark effect. In conjugated polymers, permanent dipoles may arise from charge transfer states, defects or from disorder that introduces asymmetry in the charge density along a conjugated segment.^[77,78] The shift in energy caused by a permanent dipole moment \mathbf{m}_j can be expressed as;

$$\Delta E_j^{(1)} = \mathbf{m}_j \cdot \mathbf{F} \quad (2.15)$$

For centrosymmetric non-degenerate polymers where states have no intrinsic permanent dipole moment, a second order term of the perturbation series must be considered;^[76,78,79]

$$\Delta E_j^{(2)} = \frac{1}{2}p_j F^2 \quad (2.16)$$

where p_j is called the dipole polarisability. Equation 2.16, known as the quadratic Stark effect is caused by the field-induced dipole moment states and are responsible for causing a red shift in the absorption.

The absorption spectrum is affected by both the linear and quadratic field-induced Stark effects. Combining Equations 2.15 and 2.16 allows one to obtain

the field-induced change in the transition energy, $\Delta E(F)$, and is given by;^[80]

$$\Delta E(F) = E(F) - E(0) = -(\mathbf{m}_f - \mathbf{m}_i)\mathbf{F} - \frac{1}{2}\Delta p F^2 \quad (2.17)$$

where $\mathbf{m}_f - \mathbf{m}_i$ are the dipole moments in the final excited state and the initial ground state and Δp is the variation of polarisability upon excitation.

The experimentally measured change in absorption (Equation 2.4) can be expressed in terms of ΔE as a McLaurin series;

$$\Delta\alpha = \frac{\delta\alpha}{\delta E}\Delta E + \frac{1}{2}\frac{\delta^2\alpha}{\delta^2 E}\Delta E^2 \quad (2.18)$$

The change in the field-induced absorption can be expressed in terms of the modulating electric field by inserting Equation 2.17 into 2.18. The only contribution to the first term in equation 2.18 comes from the quadratic Stark effect since isotropic averaging over randomly oriented molecules leads to $\langle \mathbf{m} \cdot \mathbf{F} \rangle = 0$. For the second term of equation 2.18, contribution from isotropic averaging of $\mathbf{m} \cdot \mathbf{F}$ must be considered. For randomly oriented dipoles, isotropic averaging of the linear Stark effect term gives;^[70]

$$\langle (\Delta\mathbf{m}\mathbf{F})^2 \rangle = \frac{1}{3}(\Delta m F)^2 \quad (2.19)$$

Considering the contributions from linear and quadratic Stark effect, the field-induced variation of the absorption is given by inserting equation 2.17 into 2.18;

$$\Delta\alpha = \frac{1}{2}\left(-\Delta p \frac{\delta\alpha}{\delta E} + \frac{1}{3}(\Delta m)^2 \frac{\delta^2\alpha}{\delta^2 E}\right)F^2 \quad (2.20)$$

A third contribution must be added to Equation 2.20 due to transfer of oscillator strength to higher lying excited states;^[79]

$$\frac{\Delta f_{ij}}{f_{ij}} = e^2 F^2 \frac{|\langle \psi_j | z | \psi_i \rangle|^2}{(E_i - E_j)^2} \quad (2.21)$$

The electroabsorption spectrum can be modelled as a linear combination of the

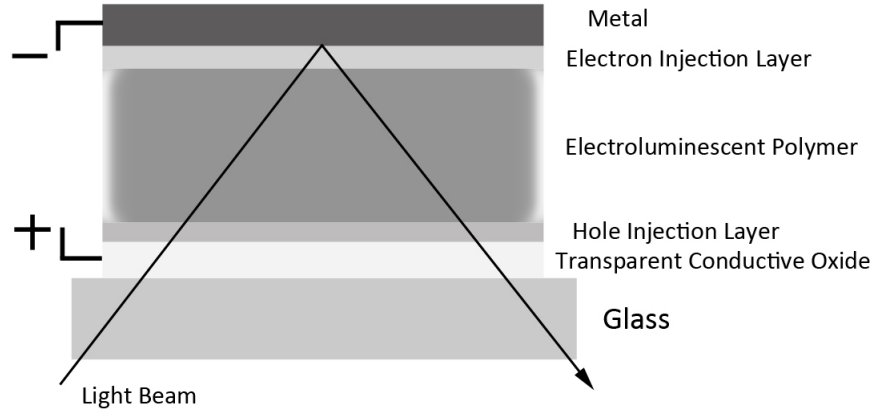


Figure 2.1: Cross-sectional view of the sample architecture used in electroabsorption experiments

absorption spectrum and its first and second derivatives by combining Equation 2.20 and 2.21;

$$\Delta\alpha = (a\alpha + b\frac{\delta\alpha}{\delta E} + c\frac{\delta^2\alpha}{\delta^2 E})F^2 \quad (2.22)$$

The electroabsorption response described by the Stark effect model for localised molecular states, predict well for conjugated polymers. In general, the electroabsorption spectra of conjugated polymers consists of all three contributions from Equation 2.22, with the relative weight of the second derivative lineshape depending greatly on the degree of disorder present in the polymer film. The above analysis points out that the electroabsorption signal is expected to have a quadratic dependence on the magnitude of the electric field, where this dependence is an important factor for extracting the built-in potential across the polymer film in PLEDs.

2.1.3 Measurement of the EA signal in conjugated polymers

The electroabsorption spectroscopy on conjugated polymers can be conducted by applying an electric field in a polymer film in a vertical electrode-polymer-electrode device structure, and by studying its electroabsorption signal. Figure 2.1 shows a cross-sectional view of the sample architecture used for electroabsorption experiments. One semitransparent electrode contact is required for light to be transmitted

through the device. The light is shone onto the PLED at an angle of 45° , while the back electrode acts as a mirror. Since the device structure required for electroabsorption spectroscopy is the same basic PLED structure, the technique allows direct comparison of the electroabsorption data with the electronic and light-emitting characteristics of the device. The main focus of the electroabsorption experiment described in this thesis was to investigate the electric field inside the polymer devices.

The electric field in the polymer layer is created by the application of a sinusoidal voltage ($V = V_{DC} + V_{AC}\cos(\omega t)$), which consists of the superposition of a DC component (F_0) and an AC component (F_{AC});

$$F = F_0 + F_{AC}\cos(\omega T) \quad (2.23)$$

The electric field in the polymer gives rise to an electroabsorption signal of the form;

$$\frac{\Delta T}{T} \cong \chi(h\nu)F^2 \quad (2.24)$$

where $\chi(h\nu)$ contains the spectral dependence. Inserting Equation 2.23 into 2.24 allows one to determine the field-induced electroabsorption response, giving the following expression;

$$\frac{\Delta T}{T} \propto \chi(h\nu) \left[F_{AC}^2 \frac{\cos(1 + 2\omega T)}{2} + 2F_{AC}F_0\cos(\omega T) + F_0^2 \right] \quad (2.25)$$

$\Delta T/T$ consists of two components: A) Fundamental harmonic frequency and B) Second harmonic frequency. Since $\Delta T/T$ is very small (10^{-7} to 10^{-4}), a phase-sensitive lock-in technique is required to measure the 1ω (in the presence of a DC field) and 2ω component of the electroabsorption signal;

$$\frac{\Delta T}{T}(h\nu, \omega) \propto 2\chi(h\nu)F_0F_{AC}\cos(\omega t) \quad (2.26)$$

$$\frac{\Delta T}{T}(h\nu, 2\omega) \propto \chi(h\nu)\frac{F_{AC}^2}{2}\cos(2\omega t) \quad (2.27)$$

Note that the DC component of the electric field, F_0 , consists of the applied DC voltage across the electrodes (F_{DC}) and also the internal or 'built-in' electric field (F_{BI}) present in the organic semiconductor where $F_0 = F_{DC} + F_{BI}$. The internal field is created in the device structure due to equilibration of the Fermi level throughout the different components of the metal-polymer-metal heterostructure. Also any space charge present in the semiconducting organic layer or at the metal-polymer interfaces can strongly influence the internal field.

2.1.4 EA in PLEDs as a probe for internal fields

Figure 2.2 shows a schematic energy level diagram of an metal-polymer-metal structure at equilibrium. Assuming that the charge density in the organic films can be low enough that the electric field across the bulk of the film is uniform,^[81,82] the expression for the size of the electric field, constant across the bulk of the active layer is given by;

$$F = \frac{V}{d} \quad (2.28)$$

and therefore the 1ω and 2ω component of the electroabsorption signal is given by;

$$\frac{\Delta T}{T}(h\nu, \omega) \propto 2\chi(h\nu)V_0V_{AC}\cos(\omega t) \quad (2.29)$$

$$\frac{\Delta T}{T}(h\nu, 2\omega) \propto \chi(h\nu)\frac{V_{AC}^2}{2}\cos(2\omega t) \quad (2.30)$$

where V_0 is the sum of the applied V_{DC} voltage (V_{DC}) and the built-in electrostatic potential (V_{BI});

$$V_0 = V_{DC} - V_{BI} \quad (2.31)$$

Mismatch between the work function of the diode's contacts creates an internal electric field ($F_{BI} = V_{BI}/d$), which is present at zero DC bias. A value for V_{BI} is determined by measuring the $\Delta T/T(1\omega)$ signal as a function of V_{DC} : i.e. when the bias at which the EA(1ω) signal vanishes.

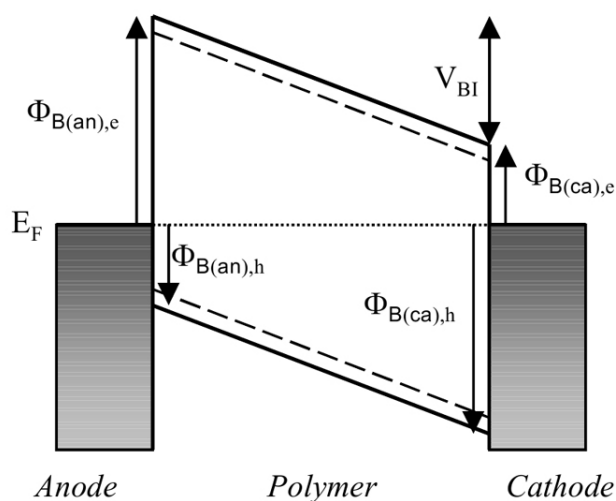


Figure 2.2: Schematic energy level diagram of an asymmetric metal-polymer-metal structure at equilibrium ($e=1$) with negligible space charge. The solid and dashed lines represent the formation energy of polarons and bipolarons, respectively. The built-in electrostatic potential (V_{BI}) and the barriers (Φ_B) to charge carriers are indicated.^[8,9]

2.1.5 The electroabsorption system setup

The electroabsorption system used for the measurements of the built-in voltage (V_{BI}) of devices in Chapter 3 has been designed and constructed by Thomas Brown.^[8] A brief summary of the design of the electroabsorption system is presented here.

A schematic diagram of the electroabsorption system is shown in Figure 2.4. A xenon arc lamp (Edinburgh Analytical Instruments Xe900) was applied as the light source, which is driven by a voltage of 33 kV and a regulated current supply of 25 A. The light produced by the lamp contains a continuous spectral distribution in the ultra-violet (UV), visible and near infrared range, which coincides with most of the spectral features of conjugated polymers for electroluminescent application. The light beam is fed into a monochromator (Bentham M300EB), featured with a 1800 lines/mm diffraction grating with a focal length of 300 mm, an aperture ratio of $f/4.2$, variable-width entrance and exit slits and a controllable wavelength from zero order to 950 nm. The monochromated beam is focused through the transparent glass/ITO anode at a degree of 45 degrees incidence, propagates through the polymer, reflected off the metal electrode then is finally collected by a lens and focused onto an amplified

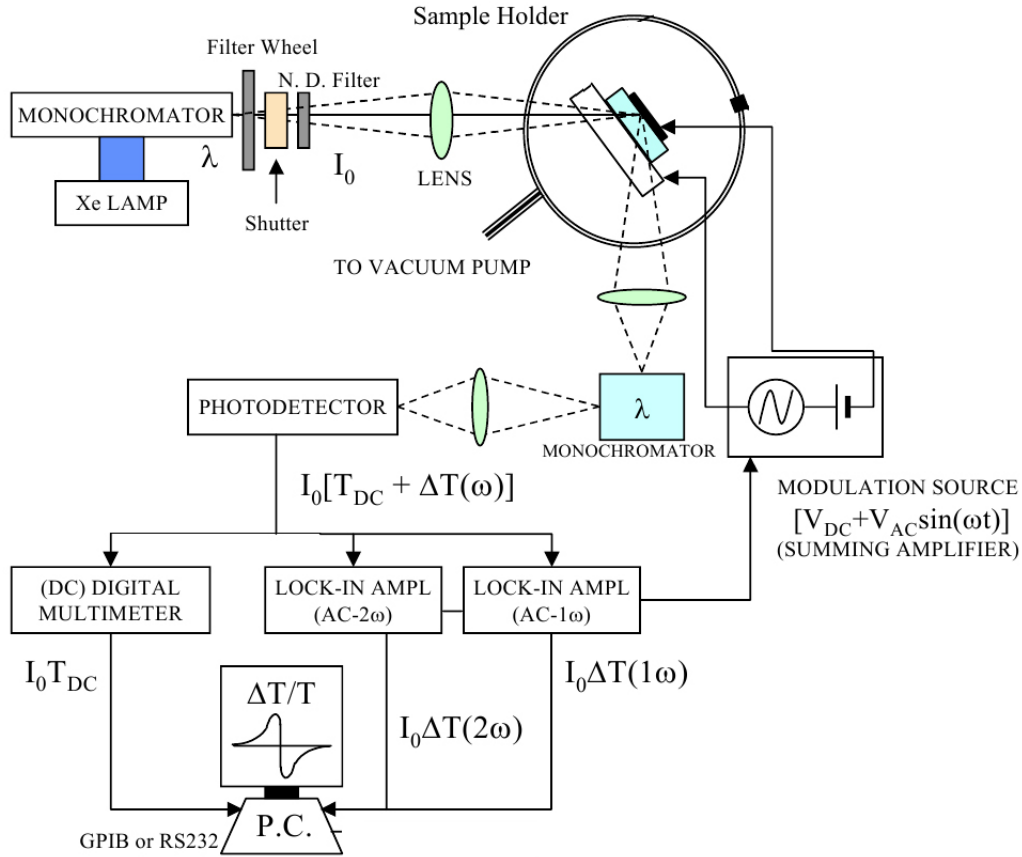


Figure 2.3: A schematic diagram of the electroabsorption system used for the measurement of the built-in voltage of electroluminescent devices in chapter 3. [8]

silicon photodiode. The Hamamatsu Photonics S1406 UV-enhanced silicon diode was employed in the set-up where it exhibited a spectral range that coincided with the monochromated light (190 nm - 950 nm). The silicon diode has a detection area of 5.7 mm^2 and is integrated with high speed operational amplifier.

A voltage bias is applied across the electrodes of the device, containing of a sinusoidal AC component of 2 kHz and a DC component. The custom made voltage modulation source was constructed with high-precision and low-noise operational amplifiers (TLC2201CP or TL051CP) and resistors. Also the voltage source consisted of two input BNC connectors (AC and DC) and one output BNC connector that generated the sum of the input biases. The electric field produced by the voltage modulation source induces a perturbation in the absorption coefficient of the polymer. The output of the photodiode is separated into a DC component (I_0T)

and an AC component ($I_0\Delta T$). The former is measured with the Keithley 199 digital multimeter and measures the DC transmission through the sample, while the latter is measured with the Stanford SR-830 lock-in amplifier and measures the perturbation in the transmission. These two data sets are transmitted to a computer where the $\Delta T/T$ ratio is calculated. Two lock-in amplifiers are used in the experiment because the electroabsorption signal is modulated both at the fundamental frequency (1ω) and at the second harmonic frequency (2ω) of the modulation voltage.

2.2 Fluorescence spectroscopy

2.2.1 Lifetime measurements in fluorescence spectroscopy

Fluorescence spectroscopy is a powerful technique that studies the luminescence characteristics of any light emitting substance. Luminescence is divided into two categories depending on the nature of the excited state. Firstly, in excited singlet states, the electron in the excited orbital is paired to the second electron in the ground-state orbital (of opposite spin). As the electron in the excited state is spin-allowed to return to the ground state, a photon is emitted. A typical lifetime of a singlet state is around 1 ns. Secondly, in triplet excited states, the electron in the excited orbital has the same spin orientation as the ground-state electron. Transitions to the ground state are forbidden and therefore a typical lifetime of a triplet state is microseconds to seconds. Time-resolved measurements are widely used in fluorescence spectroscopy as the time-resolved data may reveal two or more lifetimes, allowing the investigator to resolve the emission spectra and relative intensities of more than one states. This is particularly useful for probing the luminescence characteristics of conjugated polymers where photoexcitation is expected to produce excitons with both singlet and triplet configurations. The following paragraphs focus on methodology of time-domain fluorescence spectroscopy.

In time-domain fluorometry, the sample is excited with a pulse of light. The width of the pulse is usually much shorter than the decay time τ of the sample.

Assuming that pulse of light exciting the sample is infinitely sharp (δ -function), the excited-state population decays from an initial population n_0 of fluorophores in the excited state, with a rate $\Gamma+k_{nr}$ according to;^[83]

$$\frac{dn(t)}{dt} = -(\Gamma + k_{nr})n(t) \quad (2.32)$$

where $n(t)$ is the number of excited molecules at time t following excitation, Γ is the emissive rate, and k_{nr} is the non radiative decay rate. Since emission is a random event and each excited fluorophore has the same probability of emitting in a given period of time, the excited-state population tends to decays exponentially;

$$n(t) = n_0 \exp(-t/\tau) \quad (2.33)$$

In actual time-resolved measurements, the fluorescence intensity is observed rather than the number of excited molecules, which is proportional to $n(t)$. Therefore integrating Equation 2.32 yields an expression for a single exponential decay in terms of the time-dependent intensity $I(t)$;

$$I(t) = I_0 \exp(-t/\tau) \quad (2.34)$$

where I_0 is the intensity at time zero. The time-dependent intensity is measured after the excitation pulse. The lifetime τ is the inverse of the total decay rate which is given by;

$$\tau = (\Gamma + k_{nr})^{-1} \quad (2.35)$$

In general, the inverse of the lifetime is the sum of the rates which depopulate the excited state. The decay time τ is calculated from the slope of a plot of $\log I(t)$ versus t , or from the time at which the intensity decreases to $1/e$ of the value at $t=0$. The intensity decays are usually measured through a polariser oriented at a certain angle to avoid the effects of rotational diffusion and anisotropy of the intensity decay.

The lifetime can also be obtained by averaging the amount of time a fluorophore

remains in the excited state following excitation. This average time $\langle t \rangle$ is obtained by averaging t over the intensity decay of the fluorophore;

$$\langle t \rangle = \frac{\int_0^{\infty} tI(t)dt}{\int_0^{\infty} I(t)dt} = \frac{\int_0^{\infty} t \exp(-t/\tau)dt}{\int_0^{\infty} \exp(-t/\tau)dt} \quad (2.36)$$

Solving Equation 2.36 yields;

$$\langle t \rangle = \tau \quad (2.37)$$

Therefore the average time a fluorophore remains in the excited state is equal to the lifetime for a single exponential decay. It should be noted that the lifetime is a statistical average since fluorophores emit randomly throughout the decay. The intensity decay represents the distribution of emitted photons at different times.

For samples that exhibit multiple decay characteristics, their intensity decays are typically fit to the multiexponential model;

$$I(t) = \sum_i \alpha_i \exp(-t/\tau_i) \quad (2.38)$$

where α_i is the pre-exponential factors and $\sum_i \alpha_i$ is normalised to unity. The presence of two decay times results in curvature in the plot of $\log I(t)$ versus time. The multiexponential model allows one to resolve the decay times (τ_i) and amplitudes (α_i) of both decay components from the $I(t)$ measurements.

2.2.2 Time-correlated single photon counting

Time-correlated single photon counting (TCSPC) is the most widely used time-domain fluorescence spectroscopy.^[84] Figure 2.4 shows a diagram summarising the measurement process of TCSPC. The experiment starts with the excitation pulse, which excites the sample and starts the time measurement clock. Photons are counted digitally and are time-correlated in relation to the excitation pulse. As the sample is repetitively excited using a pulsed light source (usually a laser), a high-speed photodiode optically monitors each pulse to produce a signal which triggers the voltage ramp of a time-to-amplitude converter (TAC). The voltage ramp is

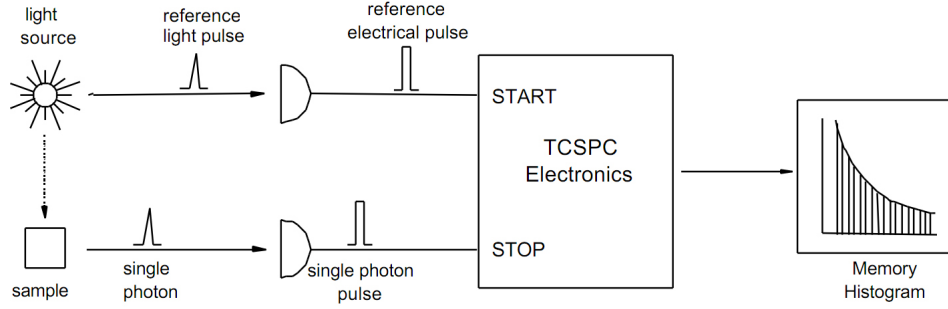


Figure 2.4: A diagram summarising the process of lifetime measurements in time-correlated single photon counting.

terminated by the first fluorescence photon from the sample, which is detected by a combination of photomultiplier and a photodiode. The subsequent output of the TAC provides a pulse voltage which is proportional to the time between the start and stop signals. A multichannel analyser (MCA) is used to convert this voltage to a time channel. After summing over numerous pulses, the MCA builds up a probability histogram of counts versus time channels. The experiment is completed when the setup has measured more than 10000 photon counts in the peak channel. The histogram of photon arrival times represents the intensity decay of the sample.

The measured intensity decay is a convolution with the illumination function.^[83] Ideally, the impulse response function $I(t)$ is a combination of δ -function excitation and a δ -function for the instrument response. However most instrument response functions are several nanoseconds wide. Hence the excitation pulse must be considered as a series of δ -functions with different amplitudes. Each of these δ -functions excites an impulse response from the sample, where the intensity is proportional to the height of the δ -function. The sum of all the exponential decays, starting with different amplitudes and a different times, is the measured function.

Each δ -function excitation is to excite an impulse response $I_k(t)$ at t_k , which is given by;^[85]

$$I_k(t) = L(t_k)I(t - t_k)\Delta t \quad (t > t_k) \quad (2.39)$$

where $L(t_k)$ is the lamp profile and the term $(t - t_k)$ appears since the impulse

response starts at $t = t_k$, and it is understood that there is no emission before excitation ($t - t_k$). The measured decay $N(t_k)$ is the sum of the impulse responses created by all the individual δ -function excitation pulses occurring until t_k ;

$$N(t_k) = \sum_{t=0}^{t=t_k} L(t_k)I(t - t_k)\Delta t \quad (2.40)$$

For small values of Δt , Equation 2.40 can be expressed as an integral;

$$N(t) = \int_0^t L(t')I(t - t')dt' \quad (2.41)$$

The experimentally measured intensity at time t is given by the sum of the intensities created by all the δ -function excitation pulses. It is assumed that there is nonzero intensity in $L(t_k)$ for the new intensity decays to be observed in the sample. Finally the convolution integral is expressed in terms of exchanged variable of integration, $t' = t - \mu$, which is given by;

$$N(t) = \int_0^t L(t - \mu)I(\mu)d\mu \quad (2.42)$$

The impulse response function $I(\mu)$ is determined according to how it best fits the experimental data.

2.3 Macroscopic kelvin probe

The Kelvin probe is a non-contact, non-destructive measurement device used to measure the work function of a conductive surface. Figure 2.5 is a circuit diagram showing the principle of the Kelvin probe measurement. The setup consists of an oscillating mesh electrode, positioned in front of the surface of material under study, which is driven by a solenoid or by piezoceramics. The mesh electrode and the surface of material can be modelled as a parallel plate capacitor in which the gap between the plates can be periodically varied. Consequently, the vibration yields an

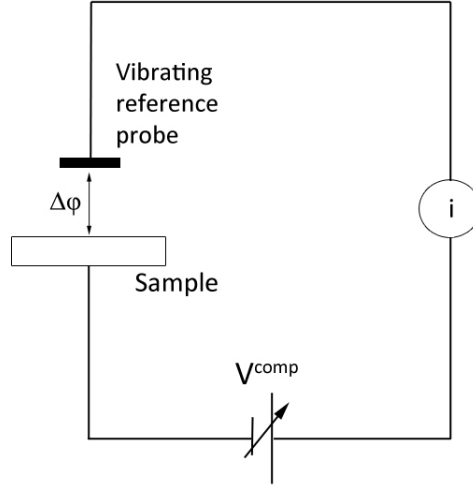


Figure 2.5: A circuit diagram of a Kelvin probe measurement. The compensation voltage V^{comp} makes up for the AC current driven by the vibrating probe.

oscillating current of the form;

$$i = \frac{dC}{dt}(e\Delta\phi - V^{comp}) \quad (2.43)$$

where V^{comp} is the external compensation voltage. The contact potential difference is formed between the two conducting plates, giving rise to $\Delta\phi$, which is equal to the difference between the work function of the surface under study (ϕ_s) and that of the reference probe (ϕ_p). The particular value of compensation voltage that can be adjusted to zero the current is the same value as the difference in work function of the two conducting plates;

$$eV_{comp} = \phi_s - \phi_p \quad (2.44)$$

In this thesis, the work function values of materials acquired from the Kelvin probe measurements are directly compared with the built-in voltage values measured from the electroabsorption spectroscopy. It should be noted that unless measurements are made in ultra-high vacuum conditions, it is difficult to find a reliable reference value for a gold mesh electrode. Depending on the state of the surface of gold, the

measured work function may vary between 4.2 eV to 5.4 eV. Ultraviolet Photoelectron Spectroscopy (UPS) is another technique that is commonly used to measure the work function of materials. It is not unusual to find the measured UPS and Kelvin Probe work function values not to agree, due to the inherent differences in the techniques themselves and the differences in the surface states of samples for each technique. Considering the difficulty in determining a reliable reference value for Kelvin Probe and the differences in comparison to UPS measurements, the Kelvin Probe is applied to measure the work function of the electrodes and charge injecting layers. Comparison of these data with known HOMO and LUMO values of electroluminescent polymer layers, and, the built-in voltage value acquired from electroabsorption technique allows us to map out the energy levels and alignment at the interfaces of the diodes.

Chapter 3

Dynamics of excitons at $\text{MoO}_{3-x}/\text{F8BT}$ and $\text{MoO}_{3-x}/\text{TFB}$ interfaces

We study the dynamics of exciton quenching in conjugated polymers due to the presence of a metal oxide contact. Using time-correlated single photon counting, the photoluminescence (PL) lifetime of F8BT and TFB single layers, and, TFB/F8BT bilayers are determined, with and without the presence of MoO_{3-x} contact. The results show that the PL lifetime of pure F8BT decreases from 1300 to 760 ps upon the presence of MoO_{3-x} contact. In contrast to F8BT, the PL lifetime of TFB is determined to be 500 ± 40 ps, with and without the presence of MoO_{3-x} contact. The TFB/F8BT bilayers exhibit biexponential decay characteristics with two lifetime values; 800 ± 50 ps and 5000 ± 400 ps, which are attributed to bulk excitonic emission and exciplex emission, respectively. Finally, the results are analysed using the energy transfer model which represents the excitons in conjugated polymers as a oscillating dipole and the MoO_{3-x} contact as the radiation absorbing mirror.

3.1 Introduction

The dynamics of excitons and charge carriers in a conjugated polymer due to the presence of a metallic film has been studied extensively in the past. Markov *et al.*^[86] investigated the dynamics of exciton quenching in a conjugated polymer due to the presence of an aluminium electrode using time-resolved photoluminescence (PL). Also the modification of PL and electroluminescence (EL) from cyano derivatives of poly(p-phenylenevinylene) (PPV) due to the proximity of gold and aluminium electrodes has been studied by Becker^[87]. Both studies have demonstrated that PL and EL of the polymer are strongly quenched within a typical distance of 15 to 20 nm from metal interfaces. Various models have been suggested for the modification of radiative decay rate of an emitter by the presence of a metal film, such as non-radiative energy transfer^[86] and interference effects.^[87] The polymer/metal interface has also been studied from the perspectives of the charge carriers and relevant interfacial electronic states. Bussac *et al.*^[88] reported that when conjugated sites of an electroactive polymer are placed a few angstroms from a metal electrode, carriers flow from the metal to these sites and remain trapped in the negative part of the image force potential. Salaneck *et al.*^[89] reported on the enhanced charge injection at the PPV/calcium junction upon the formation of interfacial oxide layer on calcium. Bipolaron energy states are known to be created at distinct polymer/metal interfaces such as PPV/calcium^[90] and F8BT/cesium,^[91] consequently reducing the rate of radiative recombination of excitons. Finally, Bäessler *et al.*^[92] reported on the mechanism of exciton quenching in conjugated polymers due to exciton splitting.

However there are few studies that explore the effects of a metal oxide film on the dynamics of excitons and charge carriers in a conjugated polymer. The incorporation of metal oxides into the PLED architecture has been a recent development, therefore it is important to investigate the mechanism of their excitonic and polaronic effects in a conjugated polymer for successful implementation. The physics of metal oxide/polymer interface is likely to be very similar to that of a metal/polymer interface, hence the motivation for this chapter is to compare, but also to differ-

entiate the physics behind both types of interface. Molybdenum trioxide has been applied as a hole injection layer in PLEDs, showing highly efficient and air-stable charge injection properties.^[60,63] Morii *et al.*^[93] demonstrated with XPS measurements, a unique chemical interaction between MoO_{3-x} and F8BT that enhanced the electroluminescent properties of PLEDs, which was only measurable when MoO_{3-x} was evaporated on top of F8BT. Our experiments further explore the interfacial physics of MoO_{3-x} /F8BT junction from excitonic perspectives. This chapter studies the dynamics of exciton quenching in a conjugated polymer due to the presence of a MoO_{3-x} contact in various sandwich structures.

Using time-correlated single photon counting (TCSPC), we measure the change in radiative lifetime of excitonic species in F8BT and TFB single layers, and, TFB/F8BT bilayers, with and without the presence of a MoO_{3-x} film. Three different thermochromic states of MoO_{3-x} film are used to obtain three different sets of radiative lifetime data from conjugated polymers in the presence of a metal oxide film. Three different types of MoO_{3-x} films were prepared by modifying their thermochromic states as follows: (a) as-deposited MoO_{3-x} , (b) post-deposition air-annealed MoO_{3-x} (or a MoO_{3-x}) and (c) post-deposition nitrogen-annealed MoO_{3-x} (or n MoO_{3-x}). Note that the dimension and fabrication specification of metal oxide/polymer structures are identical to that of PLED device structures in the following chapter, allowing us to directly compare a specific PLED performance with its corresponding radiative lifetime data. TCSPC results show a degree of decrease in radiative lifetime (upto 500 picoseconds) of F8BT depending on the presence of three thermochromically diverse MoO_{3-x} contact. However, there is no significant change in the radiative lifetime of TFB, with and without the presence of MoO_{3-x} . Finally, double-exponential decay characteristics are observed with TFB/F8BT bilayers, which is interpreted as 'exciplex' emission due to interfacial excited electronic states formed at the TFB/F8BT heterojunction. Along with the results from the previous chapter, the radiative lifetime data are used to examine the dynamics of excitonic and polaronic species at MoO_{3-x} /conjugated polymer interface.

3.2 Experimental

Time-resolved photoluminescence lifetime measurements were carried out using a commercial TCSPC setup (Edinburgh Instruments). The single polymer layer samples prepared for PL lifetime measurements consisted of a 100 nm thick film of F8BT or a 50 nm thick film of TFB on top of a spectroil, a spectroil/ MoO_{3-x} , a spectroil/a MoO_{3-x} and a spectroil/n MoO_{3-x} substrates. Additionally, spectroil/F8BT / MoO_{3-x} samples were prepared (i.e. MoO_{3-x} evaporated on top of F8BT). The bilayer samples consisted of TFB/F8BT (10nm/ 100nm) heterojunctions on top of the four substrate types used for single-layer samples. Prior to deposition, all 12 mm spectroil substrates were cleaned by ultrasonically assisted acetone bath for 15 minutes, followed by rinsing with isopropanol and then dried with nitrogen. A 25 nm thick film of MoO_{3-x} (99.999% powder, Testbourne) was thermally evaporated under high vacuum of 1×10^{-6} mbar at a deposition rate of 3 \AA s^{-1} . Post-deposition annealing of a MoO_{3-x} and n MoO_{3-x} HILs were realized on a hot plate for 3 hours at 300°C , in air and nitrogen atmosphere (inside a M-Braun glovebox), respectively. For single layer samples, a 50 nm thick film of TFB or a 100 nm thick film of F8BT was deposited by spin-coating from a 2% (w/w) toluene solution or a 2% (w/w) p-xylene solution, respectively, directly on top of MoO_{3-x} films. The TFB/F8BT bilayer samples were prepared as follows; A 10 nm thick film of TFB was deposited by spin-coating from a 2% (w/w) toluene solution directly on top of MoO_{3-x} films, and then annealed at 180°C ($< T_g$ of TFB) for 1 hr in a glovebox and cooled on a cold metal surface followed by spin-rinsing with toluene in order to remove the remaining soluble part of TFB.^[94] The latter process allows the subsequent spincoating of F8BT without the solvent dissolving the underlying TFB layer. The thickness of TFB layer before spin-rinsing with toluene was measured to be 50 nm thick with the Atomic Force Microscope (AFM). A 100 nm thick film of F8BT was spin-coated from a 2% (w/w) p-xylene solution.

For TCSPC measurements, the samples were excited with a laser beam of 371 nm in wavelength on the face of the polymer layers (except for spectroil/F8BT/ MoO_{3-x}

sample) and their photoluminescence was measured with a photodiode with 160 ps time response. The photoluminescence spectra were measured with laser pulse rate of 50 ns and the lifetime measurements were carried out with laser pulse rate of 200 ns. The photon counting for the lifetime measurements of a single layer of F8BT and a bilayer of TFB/F8BT were carried out with the monochromator passing light through at 540 nm, while for a single layer of TFB, at 435 nm.

3.3 Results

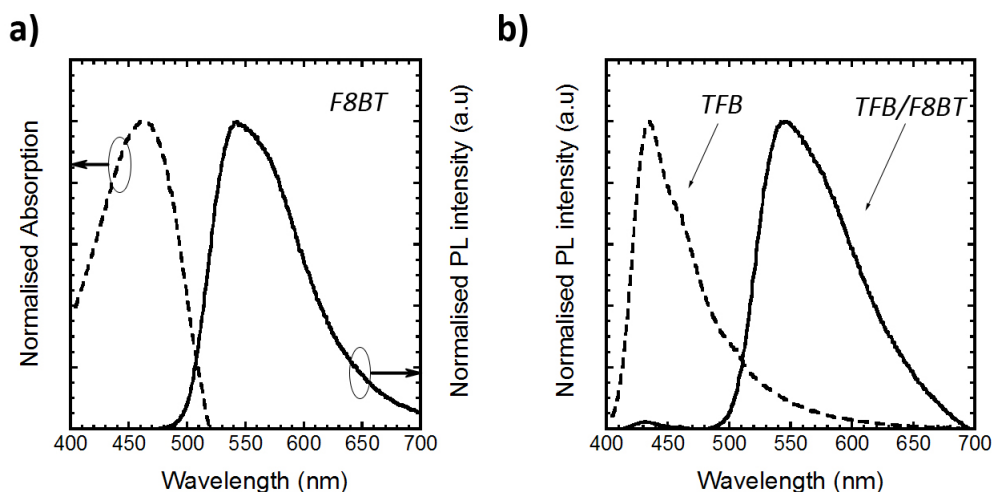


Figure 3.1: a) shows the normalised absorption (dashed line) and PL spectra (bold line) of spin-coated films of F8BT. b) shows the normalised PL spectra of spin-coated films of TFB (dashed line) and TFB/F8BT bilayers (solid line, thickness of 10 nm/100 nm).

Figure 3.1a shows the normalised absorption and PL spectra of a 100 nm-thick F8BT film on a spectro-sil substrate. The first absorption peak is centered at about 460 nm and the PL spectra consist of a single peak at 540 nm. The difference between the positions of the absorption and emission peaks indicate a Stokes shift in the magnitude of 80 nm for F8BT. Figure 3.1b shows the normalised PL spectra of a 50 nm-thick TFB film and a TFB/F8BT bilayer (10nm/100nm) on a spectro-sil. The PL spectra of a TFB film consists of a single peak at 435 nm. The PL spectra of a TFB/F8BT bilayer film consists of two emission peaks at 435 nm

and 540 nm (the former peak being much smaller). These peaks are attributed to TFB and F8BT, respectively. Figure 3.2 shows the PL decay characteristics of F8BT, MoO_{3-x} /F8BT, aMoO_{3-x} /F8BT, nMoO_{3-x} /F8BT and F8BT/ MoO_{3-x} on a spectrotil, detected at wavelength matching the PL peak of F8BT (540 nm). The excitons in F8BT exhibit single-exponential decay characteristics with varying lifetimes depending on the thermochromic state of the neighbouring MoO_{3-x} contact. The experimentally measured lifetime of excitons in a pure F8BT film is 1.309 ns, which decreases to 1.080 ns for F8BT/ MoO_{3-x} , 0.969 ns for aMoO_{3-x} /F8BT, 0.898 ns for nMoO_{3-x} /F8BT, and 0.761 ns for MoO_{3-x} /F8BT. Figure 3.3 shows the PL decay characteristics of TFB, MoO_{3-x} /TFB, aMoO_{3-x} /TFB and nMoO_{3-x} /TFB on a spectrotil, detected at wavelength matching the PL peak of TFB (435 nm). The excitons in TFB also exhibit single-exponential decay characteristics. However, unlike F8BT, the lifetime of excitons in TFB do not vary with the presence of MoO_{3-x} films. The variation in the lifetime is interpreted to be negligible and the lifetime for all four decay characteristics is calculated to be 500 ± 40 ps. Figure 3.4 shows the PL decay characteristics of TFB/F8BT, MoO_{3-x} /TFB/F8BT, aMoO_{3-x} /TFB/F8BT and nMoO_{3-x} /TFB/F8BT on a spectrotil, detected at 540 nm. These bilayer structures exhibit bi-exponential decay characteristics which are not observed in a single TFB or F8BT films. The decay characteristics can be fitted with 2 exponentials whose lifetimes are averaging at about 800 ± 50 ps and 5000 ± 400 ps, which are attributed to the bulk exciton and the exciplex state, respectively. Note that all the radiative lifetime data were obtained from the gradient of single exponential or biexponential fits to the $\log I(t)$ versus time graphs.

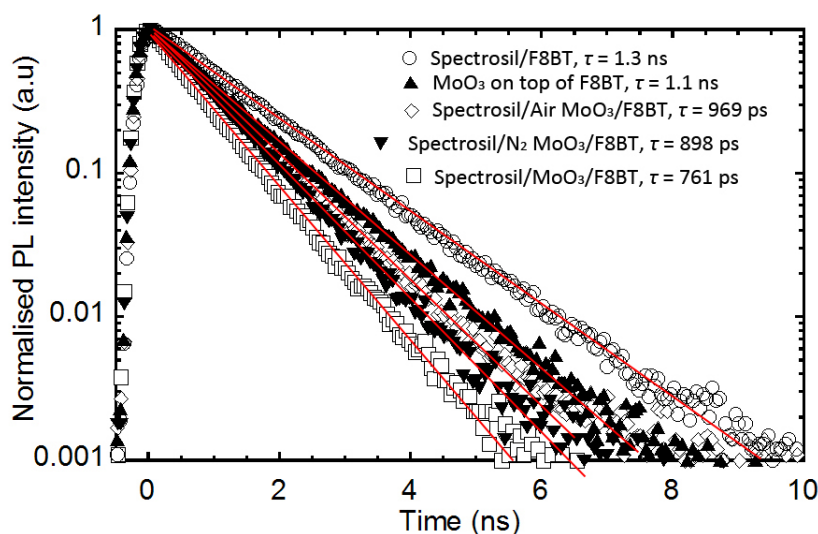


Figure 3.2: PL decay profiles of spin-coated films of F8BT, and, F8BT on top of as-deposited MoO_{3-x} , nitrogen-annealed MoO_{3-x} and air-annealed MoO_{3-x} , and, as-deposited MoO_{3-x} on top of F8BT. Samples were excited using a laser with excitation energy of 3.4 eV and PL was collected at 540 nm in wavelength. The laser beam always entered the face of F8BT (except for the sample with MoO_{3-x} on top of F8BT). Lifetimes were obtained from the gradient of single-exponential fits ($\chi^2 < 1.8$). The red lines are gradient fits at which the lifetime values were obtained.

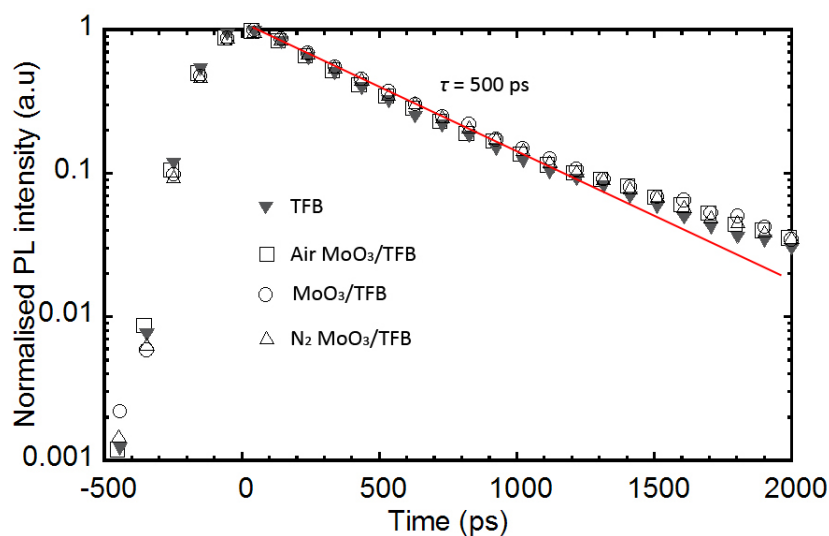


Figure 3.3: PL decay profiles of spin-coated films of TFB, and, TFB on top of as-deposited MoO_{3-x} , nitrogen-annealed MoO_{3-x} and air-annealed MoO_{3-x} . Samples were excited using a laser with excitation energy of 3.4 eV and PL was collected at 435 nm in wavelength. The average lifetime value was obtained from the gradient of single exponential fits ($\chi^2 < 10$). The red lines are gradient fits at which the lifetime values were obtained.

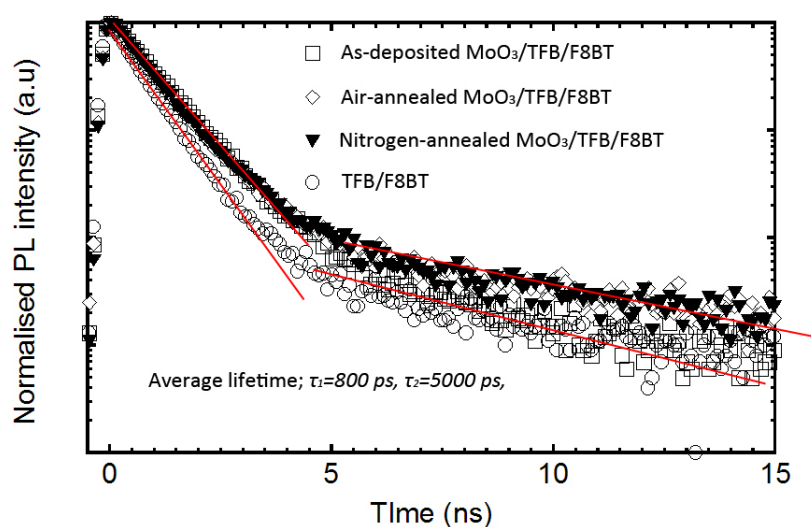


Figure 3.4: PL decay profiles of TFB/F8BT bilayers, and TFB/F8BT bilayers on top of as-deposited MoO_{3-x} , nitrogen-annealed MoO_{3-x} and air-annealed MoO_{3-x} . Samples were excited using a laser with excitation energy of 3.4 eV and PL was collected at 540 nm in wavelength. The average lifetime values were obtained from the gradient of double exponential fits ($\chi^2 < 1.2$). The red lines are gradient fits at which the lifetime values were obtained.

3.4 Discussions

3.4.1 Exciton quenching at MoO_{3-x} /F8BT interfaces

The decrease in the PL lifetime of excitons in F8BT with the presence of MoO_{3-x} films can be attributed to the increase in the rate of exciton quenching or dissociation near the MoO_{3-x} /F8BT interface. As Figure 3.2 shows, the PL lifetime of excitons in a pure F8BT film is 1.309 ns, which is reduced by nearly half of its original value, to 0.761 ns, when as-deposited MoO_{3-x} is in contact with the F8BT. Stevens *et al.*^[95] applied a photophysical modeling to femtosecond transient absorption data to identify two exciton decay mechanisms in F8BT: (a) exciton-exciton annihilation through diffusional collision and (b) exciton-exciton annihilation through Förster transfer. In the diffusional collision mechanism, the exciton encounter and collision is the rate-limiting process and the bimolecular rate constant is time independent. The latter mechanism is characterised by a bimolecular rate 'constant' that contains an explicit time dependence, where dipole-dipole interactions between pairs of excitons (or equivalent pairs) lead to a long-range resonance (Förster) energy transfer. Based on the above assumption, we propose that the lifetime of F8BT is decreased in the presence of MoO_{3-x} due to Förster energy transfer between the excitons in F8BT and the colour centres in the surface of MoO_{3-x} layer. The energy transfer model allows one to account for the modification of Förster energy transfer rate with the change in optical properties of MoO_{3-x} , which offers an explanation for different PL lifetimes observed depending on different thermochromic (or optical) states of MoO_{3-x} films.

The energy transfer model represents the emitting exciton in the bulk polymer layer as an oscillating dipole and the MoO_{3-x} layer as a partially absorbing mirror.^[96] The lifetime of an emitting dipole (or exciton) located near the absorbing MoO_{3-x} mirror can be analysed in terms of a model whose reflected electric field produces a time dependent force which is incorporated into the equation of motion of the dipole.^[97] The equation is solved to find a damping (or lifetime) term which depends on the distance of the dipole from the mirror. Considering a dipole perpen-

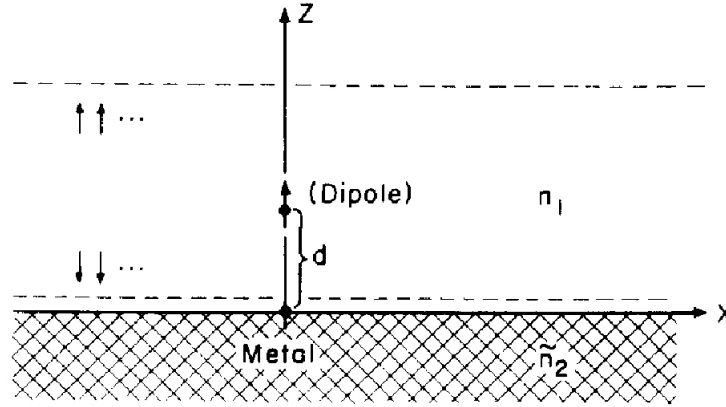


Figure 3.5: Geometry of the dipole-metal oxide mirror system for a vertical dipole; d is the distance from the dipole to the surface.^[97]

dicular to the mirror plane as shown in figure 3.5, the dipole located at a distance d from the mirror has a dipole moment given by;

$$\mu = \exp(-i\omega t - \frac{bt}{2}) \quad (3.1)$$

where $1/b$ is the lifetime of the dipole in the presence of the mirror. At large distances (equal to or greater than the wavelength of the radiation), the damping shows an oscillatory behaviour. At short distances, the damping increases (or lifetime decreases) due to non-radiative energy transfer from the dipole to the partially absorbing mirror. The total normalized damping constant can be defined as;

$$\hat{b} \equiv \hat{b}_r + \hat{b}_{et} + (1 - q) \quad (3.2)$$

where \hat{b}_r is the radiative component of the total damping constant, \hat{b}_{et} is the normalized rate constant for non-radiative energy transfer to the mirror and $(1 - q)$ represents the intrinsic non-radiative component of the total damping constant, where q is the quantum yield. Simple considerations of the dimensionality of dipole-dipole transfer predict that non-radiative energy transfer rate has a cubic dependence on

the distance between the emitter and the mirror, d , in the small distance;^[98]

$$\hat{b}_{et} = \beta d^{-3} \quad (3.3)$$

where β is the coefficient of d^{-3} or the energy transfer rate parameter. Applicable within distances of several tens of nanometer from the interface, Chance^[97] has derived an expression showing the dependence of β on the optical constants of the system;

$$\beta = \frac{3q \lambda^3 \Theta}{32 \pi^3 n_1} \frac{n_2 K_2}{(n_1^2 + n_2^2 - K_2^2)^2 + 4n_2^2 K_2^2} \quad (3.4)$$

where the dielectric containing the dipole has a real refractive index n_1 and a propagation constant $k_1 = 2\pi n_1/\lambda$, and the metal mirror has a complex refractive index $\tilde{n}_2 = n_2 + iK_2$ and a propagation constant given by $k_2 = 2\pi\tilde{n}_2/\lambda$. The quantity Θ is a parameter varying with orientation and equals 1 for a horizontal dipole, 2 for a vertical dipole, and 4/3 for a randomly oriented dipoles.

Equation 3.4 shows that the rate of non-radiative energy transfer from the emitter to the mirror is dependent on the optical constants of the two media. In our case, n_1 is the real refractive index of F8BT, n_2 is the real refractive index of MoO_{3-x} and K_2 is the imaginary part of the refractive index, or the extinction coefficient of MoO_{3-x}. Note that the extinction coefficient quantifies how fast the radiation is attenuated as it penetrates into the metal. Therefore, the extinction coefficient of the metal, along with the refractive index of the radiation propagating medium, directly alters the properties of the reflected radiation, which then changes the lifetime of the emitter. Table 3.1 shows theoretical estimates of the energy transfer rate parameter β from equation 3.4, for all MoO_{3-x}/F8BT and MoO_{3-x}/TFB interfaces. Note that β values are calculated assuming that the excitons in F8BT and TFB are emitting at a wavelength of 540 nm and 435 nm, respectively. The extinction coefficient of MoO_{3-x}, aMoO_{3-x} and nMoO_{3-x} films are determined using the simple relation;

$$K_2 = \frac{\alpha \lambda}{4\pi} \quad (3.5)$$

System	λ (nm)	n_1	n_2	K_2	β (10^{-18}cm^3)	τ (ps) (Exptl)
MoO _{3-x} /F8BT	540	1.6	2	0.43	8.22	761
nMoO _{3-x} /F8BT	540	1.6	1.6	0.25	6.36	898
aMoO _{3-x} /F8BT	540	1.6	2.4	0.44	6.24	969
MoO _{3-x} /TFB	435	2	2.2	0.86	3.24	500 \pm 40
nMoO _{3-x} /TFB	435	2	1.8	0.38	1.79	500 \pm 40
aMoO _{3-x} /TFB	435	2	2	0.40	1.71	500 \pm 40

Table 3.1: Comparison of theoretical estimates of the energy transfer rate parameter β from equation 3.4, for various MoO_{3-x}/F8BT and MoO_{3-x}/TFB interfaces. Optical constants n_1 and n_2 are taken from Ramsdale^[99] for F8BT and TFB, and from Kuhaili^[100], Hussain^[101] and Sian^[102] for all MoO_{3-x} films. We have taken $q=0.7$ and 0.55 ^[94] for F8BT and TFB systems, respectively, and the dipole is assumed to be vertical to the mirror, i.e., $\Theta=2$.

where α is the absorption coefficient of MoO_{3-x} at a specific wavelength of the emitting polymer. The thickness of thermally evaporated MoO_{3-x} films are known, therefore α was determined using the Beer-Lambert law;

$$I = I_o \exp(-\alpha x) \quad (3.6)$$

where x is the thickness of the MoO_{3-x} film, and I/I_o ratios are taken from the absorption spectra in the following chapter. Equation 3.4 exhibits an interesting resonance behaviour as shown in Figure 3.6; a plot of energy transfer rate parameter β as a function of K_2 for all MoO_{3-x}/F8BT and MoO_{3-x}/TFB interfaces. The graph illustrates a dramatic increase in the energy transfer rate at the emitter frequency at which the extinction coefficient of MoO_{3-x}, K_2 , is equal to the refractive index of the light emitting polymer, n_1 .

Along with the energy transfer mechanism as a major contributing factor to the total exciton decay process, the mechanism of diffusional collision must also be considered within our experimental context. As pointed out earlier, the non-radiative energy transfer is only applicable to excitons distributed at distances of several tens of nanometer from the polymer/metal mirror interface. For example, for the case of Al/NRS-PPV structures, the direct energy transfer to the metal is

observed within a typical distance of 7.5 nm.^[86] This causes an exciton density redistribution characterised by their diffusion length. As a consequence of stronger exciton decay occurring within a limited energy transfer range, a decrease in exciton density towards the interface is observed. Figure 3.7 shows a steady-state exciton density profiles for NRS-PPV/Al heterostructures, which illustrates the decrease in the exciton density towards the interface. The excitons diffuse into the depletion area of the exciton population at the interface, which further enhances the rate of energy transfer to the metal. Again, for the case of Al/NRS-PPV, an additional distance of 6 nm (characteristic exciton diffusion length of NRS-PPV) is contributed to the total non-radiative energy transfer range. The importance of exciton density redistribution is expected to be twofolds; A) increase in the rate of non-radiative energy transfer to the mirror and B) increase in the rate of exciton decay by diffusional collision due to bulk exciton migration towards the interface. The extent to which each of the mechanisms contributes to the total exciton decay has not been quantified in this work. Nevertheless, it should be emphasised that the non-radiative energy transfer is likely to be an important contributing factor to the total exciton decay process.

Given the above assumption and the normalised lifetime relation to the total damping term, $\hat{\tau} = 1/\hat{b}$, the theoretical estimates of β complements well with the experimentally observed PL lifetime data; i.e. greater the rate of non-radiative energy transfer lead to a lower PL lifetime of F8BT, as shown in Table 3.1. The characteristic dependence of energy transfer rate on the refractive indexes of MoO_{3-x} layers as shown in Figure 3.5 is a point of interest since the optical properties of MoO_{3-x} can be tuned by post-deposition annealing. The change in the thermochromic (and optical) properties of MoO_{3-x} is investigated in the following chapter. As-deposited films of MoO_{3-x} exhibit transparent-blue colour which becomes dark-blue when annealed in nitrogen and transparent-red colour when annealed in air. Also the complex refractive index of MoO_{3-x} films vary with their thermochromic states, which gives an explanation for the different exciton lifetimes observed for the vari-

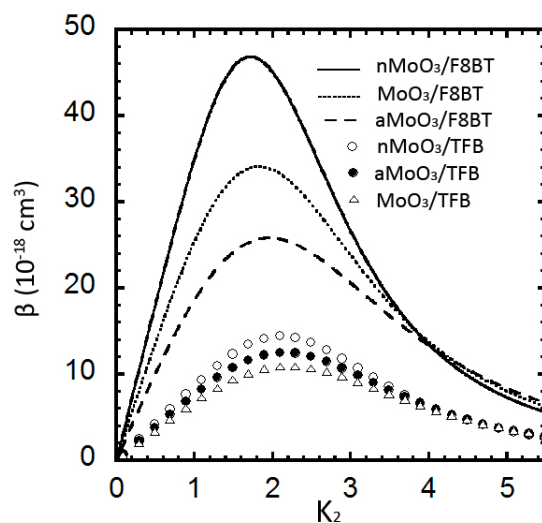


Figure 3.6: The short range energy transfer rate parameter β as a function of K_2 , the imaginary part of the refractive index of MoO_{3-x} . The dipole is assumed to be that of the F8BT and TFB excitons emitting at 540 nm and 435 nm, respectively. The refractive indexes of F8BT and TFB at the wavelength of their emittance is 1.6 and 2, respectively. The parameter β is dependent on the optical properties of the MoO_{3-x} mirror.

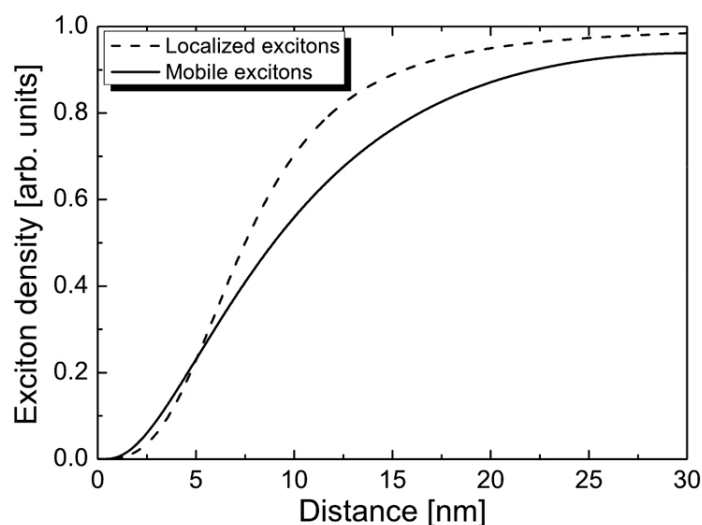


Figure 3.7: Steady-state exciton density profiles simulated for NRS-PPV/Al heterostructures.^[7]

ant configurations. The emitted radiation from the exciton is partially absorbed by the MoO_{3-x} mirrors, where the amount of that absorption is governed by their extinction coefficients. Given the right optical conditions of the media, the reflected radiation from the mirror destructively interfere with the emitting radiation, thereby

quenching the luminescence of the excitons. The relationship between the complex refractive index and the dipole radiation is further explored in the theory of non radiative and radiative surface plasmon modes.^[103]

3.4.2 MoO_{3-x} /TFB interfaces and Exciplex

In contrast to F8BT, the exciton lifetime of pure TFB does not decrease upon the application of MoO_{3-x} films as the neighbouring layers. As shown in Figure 3.3, the average exciton lifetimes of TFB in all sample configurations were determined to be 500 ± 40 ps. Therefore, the significance of non-radiative transfer between MoO_{3-x} mirrors and the TFB emitter is interpreted to be negligible for the total exciton quenching process. Given the optical conditions of the sample configurations, Table 3.1 shows that β , the non-radiative energy transfer parameter β for MoO_{3-x} /TFB interfaces, is considerably smaller than for MoO_{3-x} /F8BT interfaces. Figure 3.6 shows the dependence of β as a function of extinction coefficient K_2 of MoO_{3-x} , where it illustrates that β of MoO_{3-x} /TFB interfaces are much smaller in comparison to MoO_{3-x} /F8BT interfaces, over a wide range of K_2 values.

Figure 3.4 shows the PL decay characteristics of TFB/F8BT and all MoO_{3-x} /TFB/-F8BT on a spectrosil, detected at 540 nm. These bilayer structures exhibit biexponential decay characteristics with two exciton lifetime data, averaging at 800 ± 50 ps and 5000 ± 400 ps. The lifetime values are attributed to the bulk exciton and the exciplex states at the TFB/F8BT interface, respectively. The exciplex states in organic optoelectronic devices have been widely reported.^[104-107] The exciplex emission usually occurs in 'type-II' heterojunctions where both the HOMO and the LUMO levels of one polymer lies higher in energy than the corresponding levels in the other polymer. Depending on the energy mismatch between the frontier orbitals, type-II heterojunctions can either facilitate charge separation in photovoltaic cells or enhance quantum yields in LEDs^[106] via exothermic exciton regeneration. For the case of LEDs, there is evidence that pairs of electrons and holes accumulate as charge transfer excitons at the heterojunction. As shown in Figure 3.8, at the TFB/F8BT

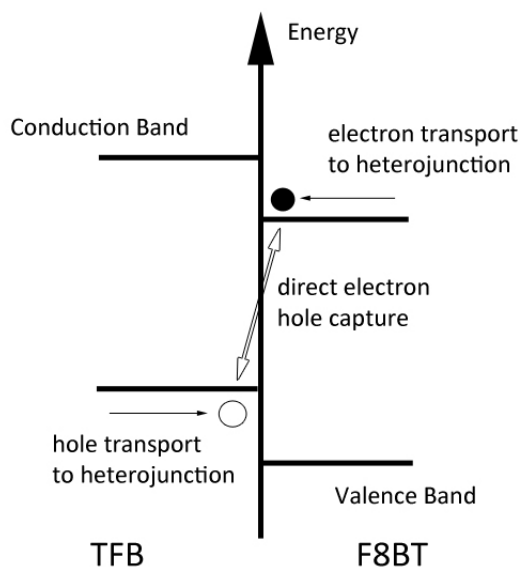


Figure 3.8: Scheme for heterojunction formed between F8BT and TFB. Electrons and holes are transported through their respective transport materials and accumulate at the heterojunction. Electron-hole capture then occurs directly without prior injection of a charge carrier into the opposite polymer.

heterojunction, electrons and holes accumulate via transportation through their respective transport materials, where electron-hole capture occurs directly without prior injection of a charge carrier into the opposite polymer. These germinate-pair recombine via an intermediate heterojunction state (termed an exciplex), which can regenerate the bulk exciton. The exciplex emission is characterised by their much increased radiative lifetime and is caused by the sufficient overlap of electron and hole wavefunctions.^[107] However, it should be mentioned that exciplex emissions are usually characterised by a red shift in the emission spectrum. This is due to the fact that the electron-hole capture and the subsequent radiative regeneration occurs at a much lower energy compared to the bulk excitonic species. Figure 3.1 shows PL spectrum of F8BT and TFB/F8BT bilayer, where it is evident that the PL spectrum of bilayer shows no or little red-shift. This can be explained by the fact that the ratio of bulk excitonic species being much larger than the exciplex states (around 1000 to 1), which has been confirmed by the amplitude of lifetime data fits.

3.5 Conclusion

In summary, we studied the dynamics of exciton quenching in conjugated polymers due to the presence of a MoO_{3-x} contact. Using time-correlated single photon counting, we measured the change in radiative lifetime of excitons in F8BT and TFB single layers, and TFB/F8BT bilayers, with and without the presence of a MoO_{3-x} contact. We prepared three different types of MoO_{3-x} films by post deposition annealing the film in air and nitrogen (the third type being as-deposited film); thereby producing MoO_{3-x} films with different optical (or thermochromic) properties. The PL lifetime data show significant decrease in radiative lifetime (upto 500 ps) of pure F8BT upon the presence of a MoO_{3-x} contact. Additionally we find that depending on the optical properties of MoO_{3-x} , the PL lifetime of F8BT is also changed. The energy transfer model is used to account the change in the non-radiative energy transfer rate at the interface of F8BT and MoO_{3-x} , with the change in complex refractive index of MoO_{3-x} films. The non-radiative energy transfer model shows that the luminescence of excitons in F8BT is quenched by the MoO_{3-x} film which acts as an absorbing mirror, where the amount of energy transfer is dependent on the complex refractive index of the radiation propagating media. This is quantified by the non-radiative energy transfer parameter β , using Chance's theoretical model. In contrast to F8BT, we find that the radiative lifetime of excitons in TFB does not change upon the presence of any type of MoO_{3-x} contact. For the case of TFB, the non-radiative energy transfer at the interface of TFB and MoO_{3-x} is assumed to be negligible to the total exciton quenching process. Finally double exponential decay characteristics are observed with TFB/F8BT bilayer samples, which is interpreted as 'exciplex' emission occurring due to interfacial electronic excitations formed at the TFB/F8BT interface.

Chapter 4

Molybdenum trioxide hole injection layers in polymer light-emitting diodes

We study the effect of post-deposition annealing molybdenum trioxide (MoO_{3-x}) hole injection layers in PLEDs on their electronic state and work function properties. We find that annealing thermally evaporated MoO_{3-x} films in air increases their hole concentration thereby improving the function of hole injection. We increase the maximum current-efficiency of ITO/ MoO_{3-x} /TFB/F8BT/Ca/Al electroluminescent devices from 1.27 cd (at 1255 cd/m^2) to 1.44 cd/A (at 3360 cd/m^2), by annealing as-deposited MoO_{3-x} HILs in air. Annealing MoO_{3-x} in nitrogen has a detrimental effect to the electroluminescent properties of devices. Finally electroabsorption spectroscopy and Kelvin probe measurements show that annealing MoO_{3-x} films results in a decrease of their work function values by 0.3 eV.

4.1 Introduction

Polymer light-emitting diodes (PLEDs) are emerging as a technology for next-generation electronic displays due to their unique properties. Performance and stability of PLEDs depends strongly on the electrodes material that interfaces the emissive semiconductor. Recently, metal oxides have been employed as charge injection layers in PLEDs architecture, showing highly efficient and air-stable charge injection properties.^[60,63,93] In those cases, MoO_{3-x} was chosen as the hole injection layer (HIL). The operating mechanism for enhanced hole injection between indium tin oxide (ITO) and organic semiconductors by applying a thin layer (<5 nm) of MoO_{3-x} has been investigated. These studies have proposed that MoO_{3-x} interlayers allow the interface to behave either as an ohmic contact,^[108] a metal-insulator-semiconductor structure,^[109] or an electron extractor.^[110] Also previous studies have investigated the work function of MoO_{3-x} films, where the measured values depend strongly upon the nature of experimental techniques and the surface states of samples used for the measurements. Kahn *et al.*^[111] measured the work function of MoO_{3-x} to be 6.7 eV by Ultraviolet Photoelectron Spectroscopy (UPS), while Murata *et al.*^[112] found the work function of MoO_{3-x} to vary from 4.9 eV to 5.9 eV with increasing film thickness from 0 to 50 nm, also by UPS. Zhu and co-workers^[113] applied contact potential difference measurement to acquire a work function value of 5.4 eV. Films of MoO_{3-x} have been studied extensively in the past for their properties of chromism, a process whereby a reversible change in the colour of a compound is induced by heat, irradiation or electric-field.^[114-118] In this chapter, we use the well-established theoretical and experimental work on chromism of MoO_{3-x} as the foundation for explaining the mechanism of hole and electronic conduction in thermally evaporated MoO_{3-x} films.

We achieve this by fabricating and characterising three different types of PLEDs, each incorporated with MoO_{3-x} HILs in different thermochromic states: (a) as-deposited MoO_{3-x} , (b) post-deposition air-annealed MoO_{3-x} (or a MoO_{3-x}) and (c) post-deposition nitrogen-annealed MoO_{3-x} (or n MoO_{3-x}). Devices are based

on bilayer of organic-solvent soluble emitters: poly((9, 9-dioctylfluorene)-alt-N-(4-butylphenyl)diphenylamine) and poly(9,9-dioctylfluorene-alt-benzothiadiazole) (TFB and F8BT). We report current and luminescence versus voltage (*JVL*) and electroabsorption^[119,120] characteristics of the three types of PLEDs with TFB/F8BT emitter (just F8BT for electroabsorption) and Ca/Al cathodes. The bias at which the electroabsorption signal is null corresponds to the difference between the electrodes' work function. We also measure the absorption spectra and work function of differently treated MoO_{3-x} films by means of UV-Vis spectroscopy and a macroscopic Kelvin probe,^[121] respectively. We find that LEDs with a MoO_{3-x} and n MoO_{3-x} HILs display drastic differences in *JVL* characteristics. Since thermochromically induced changes in optical properties of MoO_{3-x} are electronic in nature,^[115] studying the absorption spectra of representative films allows us to differentiate their electronic state. We also investigate the observed 0.2 - 0.3 eV decrease in the work function of MoO_{3-x} upon annealing, both confirmed by the built-in voltage (V_{BI}) value acquired from electroabsorption spectroscopy and Kelvin probe measurements.

4.2 Experimental

PLEDs discussed in this chapter were bilayer sandwich structure consisting of a top calcium electrode, TFB/F8BT emitting layer and an ITO/ MoO_{3-x} , an ITO/a MoO_{3-x} or an ITO/n MoO_{3-x} anode on a glass substrate. Firstly, patterned ITO substrates (Colorado Concept) were cleaned by ultrasonically assisted acetone bath for 15 minutes, followed by rinsing with isopropanol and then dried with nitrogen. A 25 nm thick film of MoO_{3-x} (99.999% powder, Testbourne) was thermally evaporated under high vacuum of 1×10^{-6} mbar at a deposition rate of 3 \AA s^{-1} . Post-deposition annealing of a MoO_{3-x} and n MoO_{3-x} HILs were realized on a hot plate for 3 hours at 300°C , in air and nitrogen atmosphere (inside a M-Braun glovebox with purity concentrations of H_2O ; < 1 ppm and O_2 ; < 1 ppm), respectively. A 10 nm thick film of TFB was deposited by spin-coating from a 2% (w/w) toluene solution directly on top of MoO_{3-x} films, and then annealed at 180°C ($< T_g$ of TFB) for 1 hr in a

glovebox and cooled on a cold metal surface followed by spin-rinsing with toluene in order to remove the remaining soluble part of TFB.^[94] The latter process allows the subsequent spincoating of F8BT without the solvent dissolving the underlying TFB layer. The thickness of TFB layer before spin-rinsing with toluene was measured to be 50 nm thick with the Atomic Force Microscope (AFM). A 100 nm thick film of F8BT was spin-coated from a 2% (w/w) p-xylene solution. Finally a 30 nm thick film of calcium cathodes and a 150 nm thick aluminium protective layers were deposited by thermal evaporation under high vacuum.

For the measurement of absorption spectra, a 200 nm thick film of MoO_{3-x} , aMoO_{3-x} and nMoO_{3-x} on spectrosil substrates were prepared by thermal evaporation followed by post-deposition annealing processes mentioned above. It should be noted that periodically varying the deposition rate during evaporation produced MoO_{3-x} films that produced deeper colour changes when annealed later, compared to films that were deposited at a constant deposition rate. We assume that periodically varying the deposition rate leads to further deviation from stoichiometry for MoO_{3-x} films and its implication on optical and electronic properties of the films will be discussed in subsequent sections.

The devices fabricated for electroabsorption spectroscopy were single-layer sandwich structure identical to the PLEDs described above except that EA devices had only F8BT as the emitter. Initially, the electroabsorption spectrum was measured for each device to identify the wavelength at which the EA response was at maximum. The probe beam was filtered through a monochromator from 320 to 640 nm. The maximum EA response (dt/T) for F8BT was found at 510 nm, measured at around 6×10^{-6} . Probing at 510 nm, the dc voltage was scanned only in the reverse bias region in order to minimise any charge injection from the cathode.

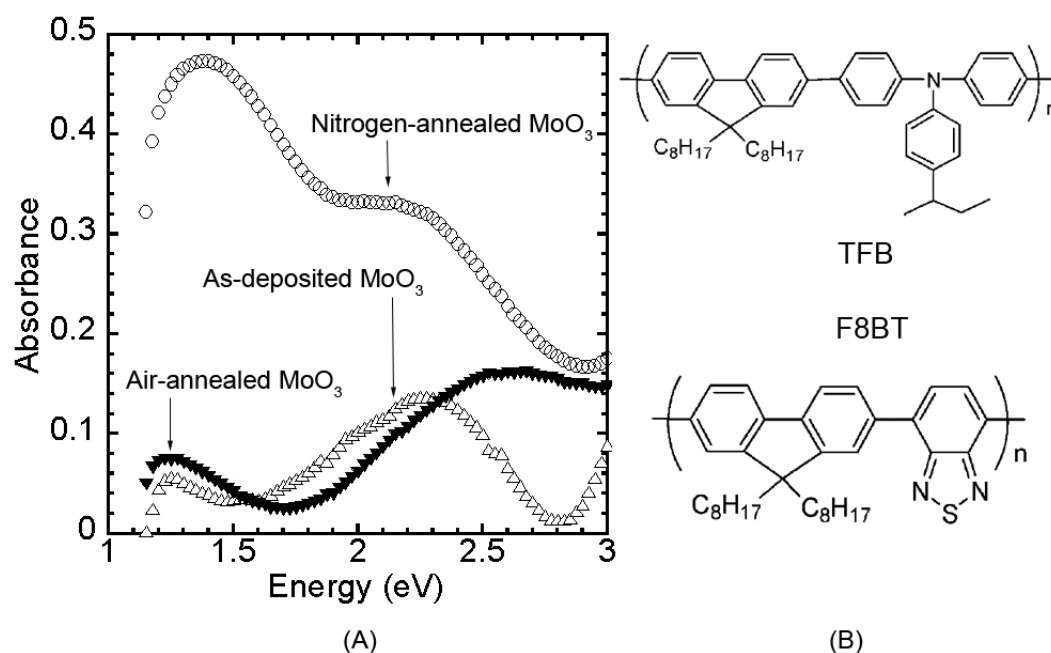


Figure 4.1: (A) Absorption spectra of 200nm-thick as-deposited MoO_{3-x} , air-annealed MoO_{3-x} and nitrogen-annealed MoO_{3-x} . (B) The chemical structure of F8BT and TFB.

4.3 Optical and electronic properties of annealed MoO_{3-x} films

Figure 4.1 shows the absorption spectra of 200 nm-thick as-deposited MoO_{3-x} , aMoO_{3-x} , and nMoO_{3-x} films on spectrosil. As-deposited films of MoO_{3-x} show absorption peaks at around 1.3 eV and 2.3 eV. Upon annealing in nitrogen, the 1.3 eV peak shifts towards 1.4 eV as the absorption coefficient increases from 10^3 to 10^4 cm^{-1} . The half width of this particular absorption band also increases by 40% upon annealing. The colour of the film changes from transparent-blue to dark-blue.

The change in the optical properties of MoO_{3-x} upon annealing in nitrogen has been extensively studied in the past and is attributed to the formation of 'molybdenum bronze' colour centers.^[118] The optical absorption is due to inter-valence charge transfer (IVCT) of localized electrons from Mo^{5+} (valence band-like) to adjacent Mo^{6+} (conduction band) cations.^[116] A similar optical absorption due to IVCT in WO_3 film is illustrated in Figure 4.2. These electrons are quasiparticles

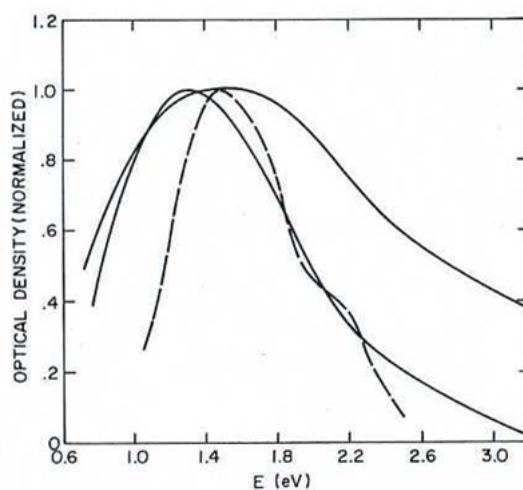


Figure 4.2: Solid lines show optical absorption bands of lightly coloured (narrow band) and heavily coloured (wide band) electrochromic amorphous WO_3 film. Lightly coloured film is 1 micron-thick and has a peak optical density of 0.45. Heavily coloured film is 0.3 micro-thick with a peak optical density of 1.8.^[116]

localized in distorted lattice sites created by their own polarization field and are termed electron-polarons.^[117] Pal *et al.* measured the dc conductivity of amorphous MoO_{3-x} films to follow a non-adiabatic small polaron hopping between Mo^{5+} and Mo^{6+} localization sites.^[122] Formation of bronzes is usually associated with the onset of metallic conductivity in transition metal oxides^[123] due to the resulting increase in electron-polaron concentration.^[124] This is further supported by the appearance of surface conductivity in otherwise insulating MoO_{3-x} films upon annealing in nitrogen. Since the conduction band of MoO_{3-x} is assumed to be originating from the d orbitals of the molybdenum cations,^[114] electron promotion from defect states associated with Mo^{5+} to the conduction band (Mo^{6+}) is likely to increase its *n*-type conductivity. Figure 4.4 a) shows a band gap diagram of MoO_{3-x} , which illustrates such electron promotion.

As Figure 4.1 shows, upon annealing the as-deposited film in air, the 2.3 eV peak shifts towards 2.6 eV, and we also observe a significant broadening of the absorption band. The colour of the film changes from transparent-blue to transparent-red. It is also possible to reversibly change the colour of previously-annealed MoO_{3-x} ; i.e.

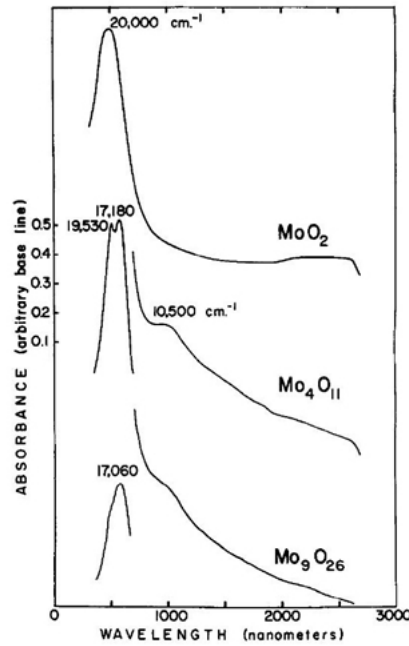


Figure 4.3: Absorption spectra of the intermediate oxide of molybdenum, showing blue-shift of the absorption peak with decreasing oxygen ratio in the compound.^[125]

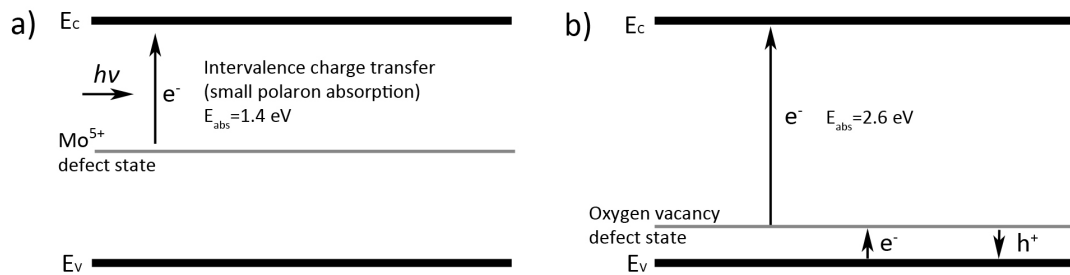


Figure 4.4: A schematic diagram showing optical absorptions occurring within the band gap of MoO_{3-x} ; a) upon annealing MoO_{3-x} films in nitrogen, Mo^{5+} defect states are created where electron promotion from these states by intervalence charge transfer to the conduction band results in increase of n -type conductivity. b) Upon annealing MoO_{3-x} in air, oxygen vacancy defect states are increased near the valence band, where electrons are promoted from the valence band to these defect states. Extra holes are created in the valence band as a result, thereby p -type conductivity of MoO_{3-x} is increased upon reducing the films.

air annealing the dark-blue MoO_{3-x} film returns its transparency and vice-versa in nitrogen atmosphere.

The absorption peak at 2.3 eV for as-deposited MoO_{3-x} is associated with the

density of oxygen vacancy defect states,^[126] since thermally evaporated MoO_{3-x} forms highly substoichiometric films due to their ionic nature.^[114] Porter *et al.*^[125] correlated the systematic blue-shift of the absorption band between 2 and 2.5 eV with increasing oxygen/metal ratio to the degree of reduction in MoO_{3-x} . Figure 4.3 shows a absorption spectra of blue-shift of the absorption peak with decreasing oxygen ratio in MoO_{3-x} films. Figure 4.1 shows a similar blue shift of the 2.3 eV absorption peak to 2.6 eV upon air annealing which we interpret as an increase in the proportion of oxygen vacancies in MoO_{3-x} . The valence band of MoO_{3-x} is a p band arising from the overlapping of the p orbitals of the oxygen ions.^[114] Recently, *p*-type conductivity has been documented in certain metal oxide systems where the defect energy levels lie proximate to the valence band of the metal oxide. In such materials, electron promotion to these defect levels creates holes in the valence band thereby increasing their *p*-type conductivity.^[127] Figure 4.4 b) illustrates such creation of holes in the valence band of MoO_{3-x} .

4.4 Surface morphology of annealed MoO_{3-x} films

Figure 4.5, 4.6 and 4.7 show AFM images of a 200 nm-thick thermally evaporated MoO_{3-x} film, a 200 nm-thick MoO_{3-x} film upon annealing in air for 3 hours at 300°C, and a 200 nm-thick MoO_{3-x} film upon annealing in nitrogen for 3 hours at 300°C, respectively. As-deposited MoO_{3-x} film exhibit much smoother and homogeneous surface morphology compared to MoO_{3-x} films annealed in air or nitrogen. It is evident that annealing MoO_{3-x} films in air or nitrogen alters the surface morphologies of the films drastically. Table 4.1 shows the root-mean-squared (RMS) roughness values acquired from each of the 20 x 20 μm AFM images. As-deposited MoO_{3-x} film has a RMS roughness of 6.2 nm, compared to 25.1 nm and 11.5 nm for air-annealed and nitrogen-annealed MoO_{3-x} films, respectively. Also air-annealed MoO_{3-x} film display greater changes in the surface morphology compared to nitrogen-annealed MoO_{3-x} film.

The increase in the roughness and alterations in the surface morphologies of

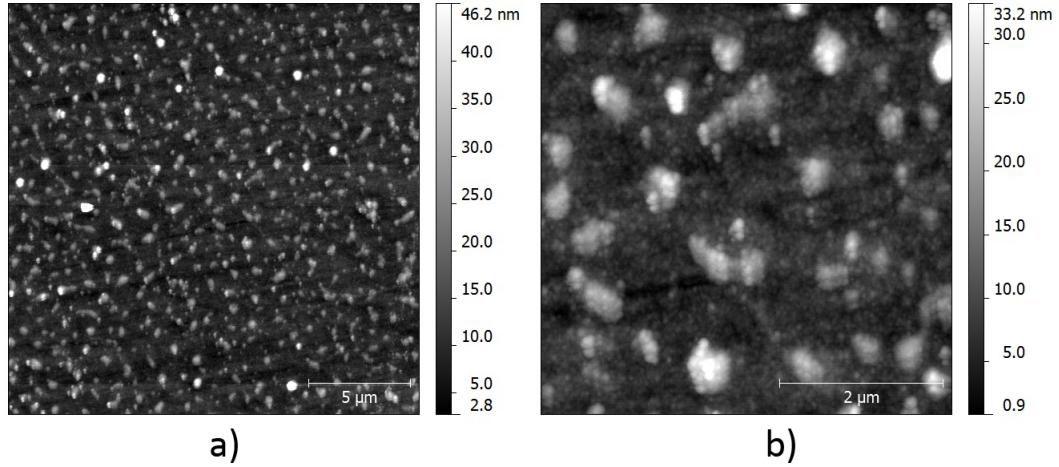


Figure 4.5: AFM images of a 200 nm-thick thermally evaporated MoO_{3-x} film; a) $20 \times 20 \mu\text{m}$ and b) $5 \times 5 \mu\text{m}$

MoO_{3-x} films upon annealing is probably due to formation of shear defects. Deng and co-workers have observed similar defect formations on MoO_{3-x} films upon a thermal reduction treatment. The study^[128] shows that thermally reducing MoO_{3-x} films have the effect of forming arrays of oxygen vacancies, whereby shear defects are created as a consequence. Such shear defects could stabilise isolated oxygen vacancies by a local transformation (shearing) from corner-connected to edge-connected MoO_{3-x} units, which then expands further by trapping more oxygen vacancies. Also the study shows that growth and size of MoO_{3-x} islands can be controlled by iterative oxidation and reduction cycles. Therefore, the difference between surface morphologies of air-annealed and nitrogen-annealed MoO_{3-x} films may be explained by the difference in the reduction processes of MoO_{3-x} films in air and nitrogen atmospheres. It is likely that more shear defects are formed on the surface of air-annealed MoO_{3-x} films (in comparison to nitrogen-annealed MoO_{3-x} films), due to a greater concentration of oxygen vacancies created during the annealing process.

4.5 Work function decrease upon annealing MoO_{3-x} films

As shown in table 4.1, the Kelvin probe measured the work function values of as-deposited MoO_{3-x} to be 5.1 ± 0.1 eV, and, 4.9 ± 0.1 eV for both a MoO_{3-x} and

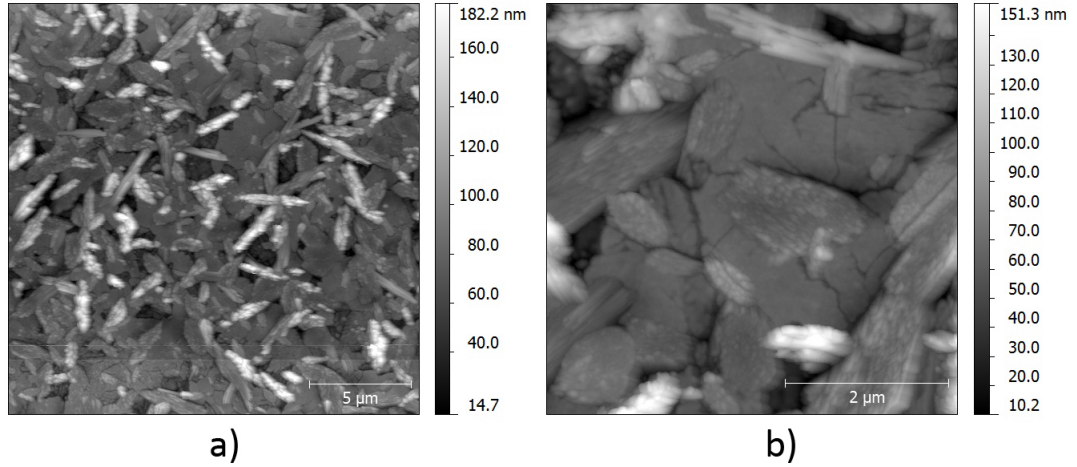


Figure 4.6: AFM images of a 200 nm-thick thermally evaporated MoO_{3-x} film upon annealing in air for 3 hours at 300°C ; a) $20 \times 20 \mu\text{m}$ and b) $5 \times 5 \mu\text{m}$

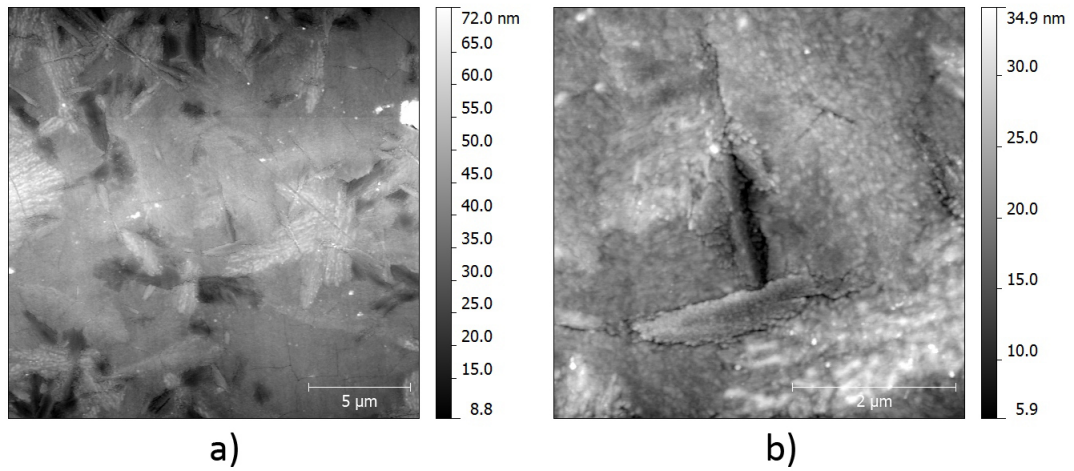


Figure 4.7: AFM images of a 200 nm-thick thermally evaporated MoO_{3-x} film upon annealing in nitrogen for 3 hours at 300°C ; a) $20 \times 20 \mu\text{m}$ and b) $5 \times 5 \mu\text{m}$

Sample	RMS Roughness (nm)
As-deposited MoO_{3-x}	6.2
Air-annealed MoO_{3-x}	25.1
Nitrogen-annealed MoO_{3-x}	11.5

Table 4.1: Table showing the root mean squared (RMS) roughness of as-deposited MoO_{3-x} , air-annealed MoO_{3-x} and nitrogen annealed MoO_{3-x} films, calculated from the AFM images.

Sample	Work Function (eV)
As-deposited MoO _{3-x}	5.1 ± 0.1
Air-annealed MoO _{3-x}	4.9 ± 0.1
Nitrogen-annealed MoO _{3-x}	4.9 ± 0.1

Table 4.2: Table showing the work function values of as-deposited MoO_{3-x}, air-annealed MoO_{3-x} and nitrogen-annealed MoO_{3-x}, measured by Kelvin Probe technique.

nMoO_{3-x}. The work function values were derived by taking a weighted mean of number of (> 5) kelvin probe measurements. The errors for these values are rather large, however this is due to the limitation of the multimeter which was used to measure the compensation potential difference between the sample and the reference of the Kelvin probe. The measured work function values are significantly lower compared to the values measured by Kahn ($\equiv 6.7$ eV).^[111] We attribute this discrepancy to the large difference in the measurement technique and the surface state of MoO_{3-x} films during the measurements. Kahn evaporated MoO_{3-x} films in a growth chamber ($\rho < 5 \times 10^{-9}$ Torr) which was connected to a ultra-high vacuum UPS analysis system ($\rho < 5 \times 10^{-10}$ Torr) that measured the work function of MoO_{3-x} films. Kahn's subsequent study^[129] shows that the work function of the same MoO_{3-x} film is decreased from 6.7 eV to 5.7 eV upon exposing the film in air for 3 minutes. Zhang *et al.*^[130] also measured the work function (UPS) of sputtered MoO_{3-x} films to decrease from 6.8 eV to 5.1 eV upon air contamination. Finally Irfan *et al.*^[131] measured the the work function (UPS) of thermally evaporated MoO_{3-x} films to decrease from 6.8 eV to 5.3 eV upon air exposure. Since our MoO_{3-x} films were exposed in air during the Kelvin Probe measurements, it is likely that surface contamination decreased the measured work function values. In further support of this hypothesis, the work function of as-deposited MoO_{3-x} films were measured after cleaning their surfaces by oxygen plasma. The measured work function increased from 5.1 eV to 5.4 eV, however upon subsequent measurements the value gradually returned to 5.1 eV after 4 hours.

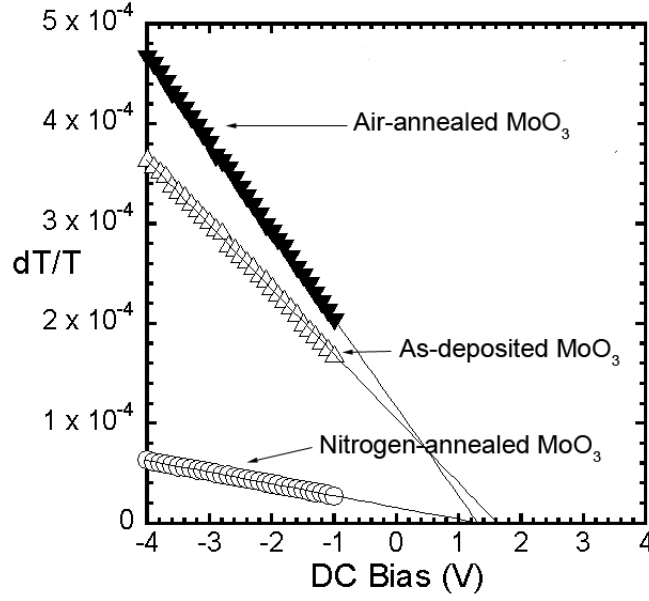


Figure 4.8: First-harmonic electroabsorption signal vs applied bias for as-deposited $\text{MoO}_{3-x}/\text{F8BT}/\text{Ca}$, $\text{aMoO}_{3-x}/\text{F8BT}/\text{Ca}$ and $\text{nMoO}_{3-x}/\text{F8BT}/\text{Ca}$ LEDs. We find $V_{\text{BI}} = 1.6 \pm 0.1$ eV for as-deposited MoO_{3-x} LEDs and $V_{\text{BI}} = 1.3 \pm 0.1$ eV for aMoO_{3-x} and nMoO_{3-x} LEDs.

Figure 4.8 displays the electroabsorption signal versus applied dc voltage for LEDs with MoO_{3-x} , aMoO_{3-x} and nMoO_{3-x} . The V_{BI} values were acquired from best line of fit at $\Delta T/T=0$. The characteristics are linear, confirming lack of charge accumulation in F8BT, and enabling determination of V_{BI} as the signal nulling voltage. We found $V_{\text{BI}} = 1.6 \pm 0.1$ V for as-deposited $\text{MoO}_{3-x}/\text{F8BT}/\text{Ca}$ and $V_{\text{BI}} = 1.3 \pm 0.1$ V for both $\text{aMoO}_{3-x}/\text{F8BT}/\text{Ca}$ and $\text{nMoO}_{3-x}/\text{F8BT}/\text{Ca}$. The observed 0.3 ± 0.1 eV decrease in the V_{BI} of LEDs with post-annealed MoO_{3-x} HILs is closely confirmed by our Kelvin probe measurements. The V_{BI} is also in good agreement with the difference between literature value of F8BT lowest unoccupied molecular orbital (LUMO), 3.5 eV,^[132] and our measured work function value of as-deposited MoO_{3-x} (5.1 eV). Using the measured work function and built-in voltage values, the energy line-up of the PLED is illustrated in figure 4.9.

The work function of MoO_{3-x} decreases by 0.2 ± 0.1 eV (or 0.3 ± 0.1 eV from V_{BI}) upon annealing in nitrogen or air. The variation in work function $\Delta\phi$ is defined

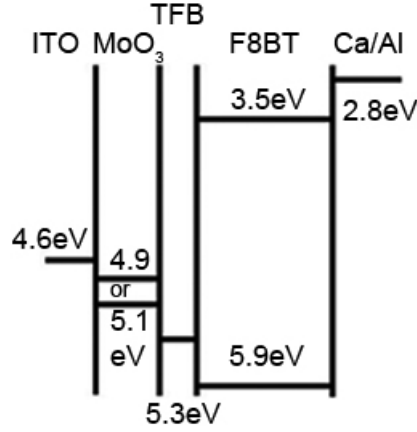


Figure 4.9: Schematic diagram of the PLEDs, showing its energy levels.

as;^[133]

$$\Delta\phi = -e\Delta V_s + \Delta\chi \quad (4.1)$$

where ΔV_s is the change in band bending at the surface and $\Delta\chi$ is the change in electron affinity of a material. According to Jacobi *et al.*,^[133] $\Delta\chi$ is caused by a modification of: (a) surface charge in surface states or resonances, (b) number of adsorbed species with a dipole moment, or (c) reconstruction of crystallographic surface structure, whereas $e\Delta V_s$ can be due to a small number of surface charge. Increase in the n -type carrier concentration at the surface of $n\text{MoO}_{3-x}$ can cause upward band bending (negative change in eV_s) which decreases the work function. The onset of surface conductivity in MoO_{3-x} after nitrogen annealing further supports this hypothesis. However we observe the same decrease of work function in $a\text{MoO}_{3-x}$ which cannot be accounted for by band bending alone since increase in hole concentration would cause a downward band bending. Hence the principal factor in the decrease of work function for both $a\text{MoO}_{3-x}$ and $n\text{MoO}_{3-x}$ is likely to be due to reconstruction of crystallographic surface structure to a higher degree of order by annealing. Such reconstruction diminishes electron scattering in the space charge region which in turn, lowers the work function (as observed with zinc oxide films upon annealing).^[134]

Device	V_{on} [V]	L_{max} [cd/m ²]	Max EQE [%]	η_{max} [cd/A]
As-deposited MoO _{3-x}	4.3	2728	0.42	1.27
Air annealed MoO _{3-x}	3.6	5615	0.48	1.44

Table 4.3: Table showing efficiency characteristics of ITO/MoO_{3-x}/TFB/F8BT/Ca/Al devices with as-deposited MoO_{3-x} and air annealed MoO_{3-x} hole injection layers (V_{on} is turn on voltage, L_{max} is maximum luminescence, EQE is external quantum efficiency and η_{max} is maximum current efficiency).

4.6 Current-Light-Voltage characteristics of PLEDs

Figure 4.10 shows the *JVL* curves of LEDs with as-deposited MoO_{3-x}, aMoO_{3-x} and nMoO_{3-x} HILs. LEDs with as-deposited MoO_{3-x} HIL exhibit maximum luminescence of 2730 cd/m² (at 0.73 cd/A) and maximum current-efficiency of 1.27 cd/A (at 1255 cd/m²), while LEDs with aMoO_{3-x} HIL improves the maximum luminescence to 5680 cd/m² (at 1.16 cd/A) and maximum current-efficiency to 1.44 cd/A (at 3360 cd/m²). As discussed in section 4.3, upon reducing MoO_{3-x} films by annealing in air, defect levels associated with oxygen vacancies are created in the forbidden energy gap close to the valence band. The superior performance of PLEDs (or enhancement of hole injecting properties) with an aMoO_{3-x} HIL is attributed to the increase in *p*-type conductivity caused by extra holes created in the valence band of aMoO_{3-x}. Table 4.3 compares the efficiency characteristics of PLEDs with as-deposited MoO_{3-x} and aMoO_{3-x}.

Interestingly, LEDs with nMoO_{3-x} HILs are not luminescent at all, although they display extremely high current-density (10 mA/cm² at a voltage of 2 V) compared to the other LEDs. It is difficult to pin-point a definite answer for such observation. It is possible that devices with nMoO_{3-x} HILs may short circuit due to mal-functional contact within the device caused by increase in the roughness of nMoO_{3-x} upon annealing. However, as the RMS roughness data shows for 200 nm-thick MoO_{3-x} films, annealing the films in air produced films with higher RMS roughness values (25.1 nm for aMoO_{3-x} and 11.5 nm for nMoO_{3-x}). Although devices with aMoO_{3-x} HILs

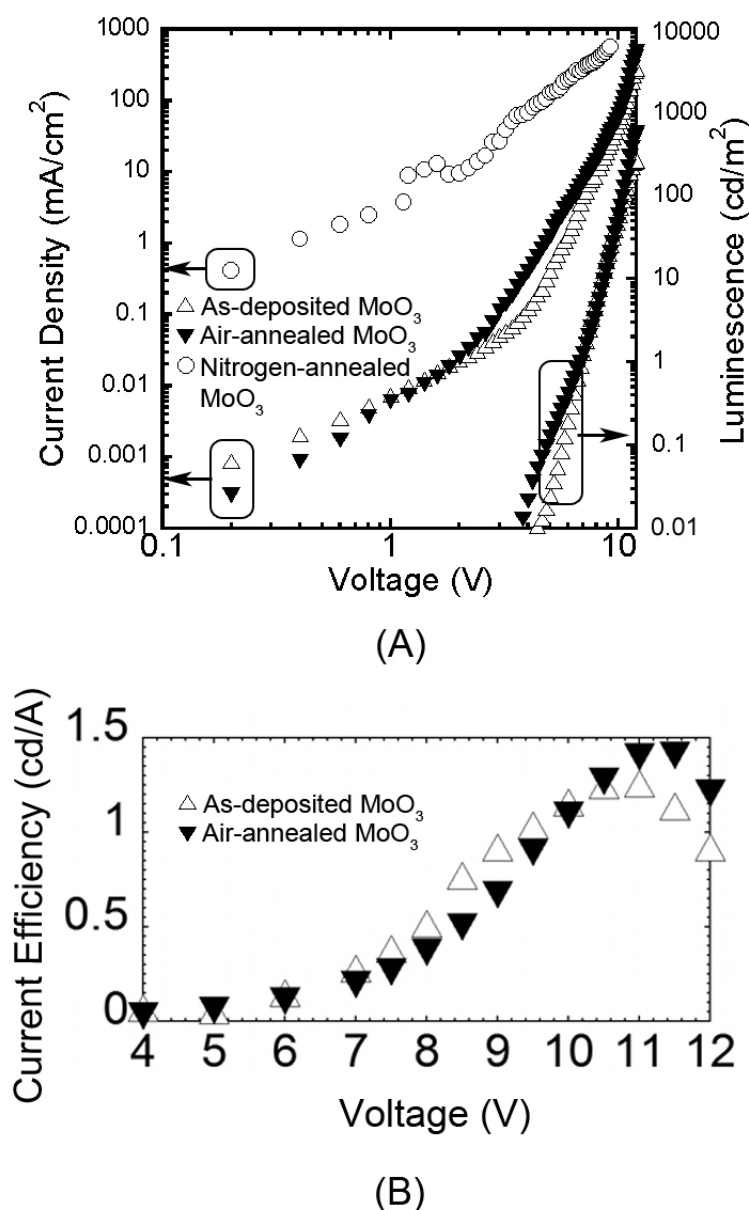


Figure 4.10: (A) Current and luminescence versus voltage (*JVL*) characteristics for ITO|HIL|TFB|F8BT|Ca|Al devices where HIL is either as-deposited MoO_{3-x}, air-annealed MoO_{3-x} or nitrogen-annealed MoO_{3-x}. (B) Current efficiency versus voltage for as-deposited MoO_{3-x} and air-annealed MoO_{3-x} LEDs.

exhibited the best *JVL* characteristics. Another possibility is that nMoO_{3-x} HIL may dope the TFB layer, thereby interfering with the hole-injecting and electron-blocking functionality of the TFB layer. Such doping process may have occurred during the fabrication process (while spin-casting TFB^[94]), where the interfaces of nMoO_{3-x}/TFB were heated to 180 °C. However note that the other two types of

devices were subjected to exactly the same fabrication procedures (except for the preparation of HILs), however they exhibited normal *JVL* characteristics.

4.7 Conclusion

In summary, we experimented with post-deposition annealing the MoO_{3-x} hole injection layers in PLEDs, subsequently investigating into the effect of annealing on their hole injection and work function properties. Application of thermally evaporated MoO_{3-x} and post-deposition annealed (in air and nitrogen) MoO_{3-x} films as hole injection layers allowed us to compare the characteristics of three different types of PLEDs. The current and luminescence versus voltage characteristics shows that PLEDs with air-annealed MoO_{3-x} HILs exhibit highest luminescence and current efficiency, while PLEDs with nitrogen-annealed MoO_{3-x} HILs are not luminescent at all. By studying the absorption spectra of MoO_{3-x} films, we attribute the high current-luminescence efficiency of the device to the increase in *p*-type conductivity of air-annealed MoO_{3-x} HIL, while annealing the MoO_{3-x} film in nitrogen has a detrimental effect to the luminescent properties of the device. Finally electroabsorption spectroscopy and Kelvin probe measurements show that upon annealing MoO_{3-x} films in any atmosphere, the work function decreases by 0.3 eV.

Chapter 5

Conclusion and outlook

This chapter presents a brief summary of the findings in the thesis and the performance of PLEDs characterised in Chapter 4 is analysed based upon the properties of MoO_{3-x} and MoO_{3-x} /polymer interfaces studied in Chapter 3 and 4. Finally future work regarding the application of MoO_{3-x} in PLEDs are suggested.

5.1 Summary of the findings

The thesis investigated the application of MoO_{3-x} as hole injection layers (HILs) in PLEDs. Recent applications of metal oxides into the PLED architecture has been motivated by the benefits of protection against the intrusion of oxygen and water into PLEDs that tends to decompose conjugated polymers, as well as enhanced device performances. The performance of MoO_{3-x} HILs in PLEDs is investigated by fabricating ITO/ MoO_{3-x} /TFB/F8BT/Ca/Al electroluminescent devices and characterising their efficiency and luminescence properties by various experimental techniques. Device performance is studied in connection with various physical properties of MoO_{3-x} films, experimentally measured as a separate material component.

Chapter 3 studies the dynamics of exciton quenching in conjugated polymers due to the presence of MoO_{3-x} contact. Using time-correlated single photon counting, the photoluminescence (PL) lifetimes of F8BT and TFB single layers, and TFB/F8BT bilayers were determined, with and without the presence of MoO_{3-x} contact. We find that the PL lifetime of excitons in pure F8BT is decreased by 500 picoseconds upon the application of MoO_{3-x} as the neighbouring contact. In contrast to F8BT, the PL lifetime of excitons in pure TFB does not decrease upon the application MoO_{3-x} contact. The non-radiative energy transfer model is employed to quantitatively analyse the data. The model represents the excitons in conjugated polymers as a dipole emitter and the MoO_{3-x} contact as a radiation absorbing mirror. The theory allows us to calculate the non-radiative energy transfer rate parameter β which quantifies the amount of exciton quenching caused by the absorption of energy from the excitonic emitter to the absorbing MoO_{3-x} mirror. By measuring the PL lifetime of F8BT and TFB in contact with three different types of MoO_{3-x} prepared by post-deposition annealing the film in nitrogen and air, we find that the amount of exciton quenching is governed by the complex refractive index of the MoO_{3-x} . Since annealing MoO_{3-x} films modifies their optical properties, using the absorption spectra from the previous chapter we calculate values of β per each MoO_{3-x} /conjugated polymer interfaces. The calculated β values correlates

well with the experimentally observed PL lifetimes.

Chapter 4 presents the fabrication and characterisation of three different types of PLEDs, each applied with MoO_{3-x} HILs with varying optical and electronic properties. This is achieved by post-deposition annealing MoO_{3-x} in air and nitrogen to modify their physical properties and subsequently using them as HILs. By studying the absorption spectra of MoO_{3-x} in context with the thermochromic properties of MoO_{3-x} , we find that post-deposition annealing MoO_{3-x} in air has the effect of increasing their hole concentration. This improves the role of MoO_{3-x} as hole injection layers in PLEDs. Upon annealing the as-deposited MoO_{3-x} HILs in air, we improve the maximum current efficiency of PLEDs from 1.27 cd/A (at 1255 cd/m²) to 1.44 cd/A (at 3360 cd/m²), as well as increasing the maximum luminescence from 2723 cd/m² to 5680 cd/m². PLEDs employed with nitrogen annealed MoO_{3-x} HILs were not luminescent at all. We attribute this to increase of electron concentration in MoO_{3-x} upon annealing in nitrogen, which has a detrimental effect on their role as hole injection layers. Finally the macroscopic Kelvin probe and electroabsorption spectroscopy measurements show that annealing MoO_{3-x} films in any atmosphere has the effect of decreasing their work function by 0.3 eV. We attribute the finding to reconstruction of crystallographic surface structure to a higher degree of order by annealing, which diminishes electron scattering in the space charge region.

5.2 Application of ITO/ MoO_{3-x} /TFB as anodes in electroluminescent devices

In this thesis, the application of ITO/ MoO_{3-x} /TFB structure as the anode to F8BT electroluminescent polymer has been the key recipe to achieving PLEDs with high luminescence and current efficiency. The PLEDs studied prior to the one presented in this thesis were fabricated without the TFB layer (i.e. ITO/ MoO_{3-x} /F8BT/Ca/Al), otherwise treated to exactly the same fabrication methods. Upon the application of TFB into the device architecture, the maximum luminescence increased from 4 cd/m² to 5680 cd/m², as well as improving the current efficiency by a similar order

(data of prior devices are not included in this thesis). By studying the properties of MoO_{3-x} films and MoO_{3-x} /conjugated polymer interfaces, we may explain the improvement in device performances.

As mentioned in the previous section and Chapter 4, post-deposition annealing thermally evaporated MoO_{3-x} films in air has the effect of increasing the hole concentration in the films, thereby improving their hole injection properties. However prior devices fabricated with MoO_{3-x} /F8BT interfaces exhibited poor luminescent characteristics. Chapter 4 investigated the dynamics of exciton quenching at the MoO_{3-x} /F8BT interfaces, where we find that non-radiative energy transfer rate between MoO_{3-x} /F8BT interfaces are greater in comparison to MoO_{3-x} /TFB interfaces (see Table 3.1 on page 53 and Figure 3.2 and 3.3 on page 48 and 3.6 on page 55) Therefore we interpret that the poor performance of devices fabricated with MoO_{3-x} /F8BT interfaces are due to the increase in the rate of exciton quenching in F8BT upon the presence of MoO_{3-x} contact.

Application of a thin layer of TFB between MoO_{3-x} and F8BT has two performance altering consequences. Firstly the non-radiative energy transfer at the interfaces of MoO_{3-x} and TFB is assumed to be negligible compared to the MoO_{3-x} /F8BT interfaces. Also the energy transfer model is only applicable to the dipole emitters and absorbing mirror at a short distance of tens of nanometer. Therefore the application of 10 nm of TFB layer acts as a energy transfer buffer layer between MoO_{3-x} and F8BT, as well as their own excitonic processes not being affected by the MoO_{3-x} contact. Secondly excitons with longer lifetime of 5000 ps are created (in comparison to the average bulk exciton lifetime of F8BT; 800 ps), upon the application of TFB layer due to the formation of exciplex states at the TFB/F8BT interfaces. These two factors contribute to improving the device performance, where the maximum luminescence of devices increases by an order of more than thousand times upon the application of TFB layer between MoO_{3-x} and F8BT layers.

5.3 Suggestions for future work

Application of MoO_{3-x} in conjugated polymer based devices promises numerous approaches in which the performance of devices can be improved, and the research is already showing some sign of success. As already mentioned in section 1.7, MoO_{3-x} have been applied as hole injection layers in PLEDs and solar cells, as well as a connecting structure for tandem devices. It is important to study the electronic properties of MoO_{3-x} and the physics of MoO_{3-x} /conjugated polymer interfaces in device contexts, in order to make further technological leaps in the field electrode engineering. Based on the findings of this thesis, we make the following suggestions for future work.

- Application of nitrogen-annealed MoO_{3-x} films as electron injection layers in PLEDs
- Annealing of MoO_{3-x} films in other reducing atmosphere to further increase hole concentration
- Systematic variation of the refractive index of MoO_{3-x} by annealing the films in various conditions
- Investigating the effect of change in refractive index of MoO_{3-x} on the rate of exciton quenching in F8BT

In Chapter 4, thermally-evaporated MoO_{3-x} films were annealed in nitrogen which resulted in the onset of metallic conductivity. This is attributed to the formation of molybdenum bronze, otherwise termed 'molyblue'. Devices applied with nitrogen annealed MoO_{3-x} HILs were not luminescent at all due to their poor hole injection properties. However future work is suggested whereby 'nitrogen-annealed' MoO_{3-x} films are used as electron injection layers instead as hole injection layers. Considering that LUMO of F8BT is 3.5 eV and the conduction band of MoO_{3-x} is 2.3 eV,^[62] electrons injected from MoO_{3-x} into F8BT may not require to overcome an energy barrier. However nitrogen-annealed MoO_{3-x} films are coloured blue and

therefore less transparent for visible spectrum. Also it may be necessary to map out the Fermi level and the band gap of MoO_{3-x} and its post deposition annealed counterparts to seriously consider applying them as electron injection layers.

Air-annealed MoO_{3-x} films performed better as hole injection layers due to the increase of hole concentration. For future work, we suggest annealing MoO_{3-x} films in other potential reducing atmospheres such as hydrogen, vacuum or innate gases. We proposed that the increase of hole concentration in MoO_{3-x} films was caused by creation of oxygen vacancy defect states near the valence band, consequently creating holes in the valence band due to electron promotion to the defect states. It may be possible to further increase the concentration of holes by experimenting to find a more suitable reducing atmosphere other than air.

In Chapter 3, we find that the complex refractive index of MoO_{3-x} directly modifies the rate of exciton quenching (or non-radiative energy transfer) at the MoO_{3-x} /conjugated polymer interfaces. The extinction coefficient of MoO_{3-x} governs the propagation distance of radiation from the excitons into the MoO_{3-x} films, therefore the amount of energy transferred. Future work is suggested whereby the complex refractive index of MoO_{3-x} films are systematically varied by annealing the films in various conditions. We found that the annealing temperature, duration and atmosphere has a great influence on the optical properties of MoO_{3-x} films. Therefore it may be possible to produce MoO_{3-x} films with different refractive index values by annealing the films in set of different durations (1, 2, 3, 4 hours and so on) and set of different temperatures (200, 300, 400 °C and so on). Also the conditions in which MoO_{3-x} films are thermally evaporated has a great effect on their optical properties. The refractive index of MoO_{3-x} films may be modified by thermally evaporating them in various deposition rates as well as varying the deposition rate during deposition. Application of ellipsometry would be essential to measure the complex refractive index of MoO_{3-x} accurately.

Subsequently, the effect of change in optical properties of MoO_{3-x} on the dynamics of excitons at the MoO_{3-x} /conjugated polymer interfaces may be studied in

further detail. Since non-radiative energy transfer rate β between the polymer layer and MoO_{3-x} is dependent on the extinction coefficient of MoO_{3-x} . The change in rate of exciton quenching may be determined upon the application of MoO_{3-x} films with a set of different refractive index values.

Chapter 6

Bibliography

Bibliography

- [1] J. H. Burroughes, D. D. C. Bradley, A. R. Brown, R. N. Marks, K. Mackay, R. H. Friend, P. L. Burn, and A. B. Holmes. *Nature*, 347:539, 1990.
- [2] N. C. Greenham, S. C. Moratti, D. D. C. Bradley, R. H. Friend, and A. B. Holmes. *Nature*, 365:628, 1993.
- [3] J. R. Sheats, H. Antoniadis, M. Hueschen, W. Leonard, J. Miller, R. Moon, D. Roitman, and A. Stocking. *Science*, 273:884, 1996.
- [4] I. H. Campbell, P. S. Davids, D. L. Smith, N. N. Barashkov, and J. P. Ferraris. *Appl. Phys. Lett.*, 72:1863, 1998.
- [5] R. H. Friend, R. W. Gymer, A. B. Holmes, J. H. Burroughes, R. N. Marks, C. Taliani, D. D. C. Bradley, D. A. Dos Santos, J. L Brédas, M. Logdlund, and W. R. Salaneck. *Nature*, 397:121, 1999.
- [6] F. Cacialli. *Phil. Trans. R. Soc. Lond. A*, 358:173, 2000.
- [7] Denis E. Markov. *Excitonic processes in polymer-based optoelectronic devices*. PhD thesis, University of Groningen, 2006.
- [8] Thomas M. Brown. *Electroabsorption investigations of polymer light-emitting diodes with efficient electrodes*. PhD thesis, University of Cambridge, 2001.
- [9] I. H. Campbell and D. L. Smith. *Solid State Physics; Vol. 55*. Academic Press, San Diego, 2001.
- [10] H. Bäessler. *Phys. Status Solidi B*, 175:15, 1993.

- [11] Y. N. Garstein and E. M. Conwell. *Chem. Phys. Lett*, 245:351, 1995.
- [12] A. Ioannidis, E. Forsythe, Y. Gao, M. W. Wu, and E. M. Conwell. *Appl. Phys. Lett.*, 72.
- [13] E. M. Conwell and M. W. Wu. *Appl. Phys. Lett.*, 70:1867, 1997.
- [14] P. W. M. Blom and M. C. J. M. Vissenberg. *Phys. Rev. Lett.*, 80:3819, 1998.
- [15] H. Meyer, D. Haarer, H. Naarmann, and H.H. Hörhold. *Phys. Rev. B*, 52:2587, 1995.
- [16] J. L. Brédas, J. Cornil, and A. J. Heeger. *Adv. Mat.*, 8:447, 1996.
- [17] R. N. Marks, J. J. M. Halls, D. D. C. Bradley, R. H. Friend, and A. B. Holmes. *J. Phys. Cond. Matter*, 6:1379, 1994.
- [18] N. C. Greenham and R. H. Friend. *Solid State Phys.: Vol. 49*. Academic Press, San Diego, 1995.
- [19] J. S. Wilson, A. S. Dhoot, A. J. A. B. Seely, M. S. Khan, A. Kohler, and R. H. Friend. *Nature*, 413:828, 2001.
- [20] R. H. Friend F. Cacialli, N. Haylett, R. Daik, W. J. Feast, D. A. Dossantos, and J. L. Brédas. *Appl. Phys. Lett.*, 69:3794, 1996.
- [21] B. K. Crone, P. S Davids, I. H. Campbell, and D. L. Smith. *J. Appl. Phys.*, 87:1974, 2000.
- [22] P. W. M. Blom, M. J. M. de Jong, and J. J. M. Vleggaar. *Appl. Phys. Lett.*, 68:3308, 1996.
- [23] L. Bozano, S. A. Carter, J. C. Scott, G. G. Malliaras, and P. J. Brock. *Appl. Phys. Lett*, 74:1132, 1999.
- [24] I. H. Campbell, T. W. Hagler, D. L. Smith, and J. P. Ferraris. *Phys. Rev. Lett*, 76:1900, 1996.

- [25] S. Naka, M. Tamekawa, T. Terashita, H. Okada, H. Anada, and H. Onnagawa. *Synth. Metals*, 91:129, 1997.
- [26] I. H. Campbell and D. L. Smith. *Appl. Phys. Lett.*, 74:561, 1999.
- [27] I. D. Parker. *J. Appl. Phys.*, 75:1656, 1994.
- [28] S. M. Sze. *The Physics of Semiconductor Devices, Chapter 3 : Metal-Semiconductor Contact*. Wiley, New York, 1969.
- [29] G. L. J. A. Rikken, D. Braun, E. G. J. Staring, and R. Demandt. *Appl. Phys. Lett.*, 65:219, 1994.
- [30] U. Wolf, V. I. Arkhipov, and H. Bäassler. *Phys. Rev. B*, 59:7507, 1999.
- [31] Y. N. Garstein and E. M. Conwell. *Chem. Phys. Lett.*, 255:93, 1996.
- [32] H. Vestweber, J. Pommerehne, R. Sander, R. F. Mahrt, A. Greiner, W. Heitz, and H. Bässler. *Synth. Metals*, 68:263, 1995.
- [33] K. Seki and M. Tachiya. *Phys. Rev. B*, 65:14305, 2001.
- [34] R. A. Marcus. *J. Chem Phys.*, 81:4494, 1984.
- [35] R. A. Marcus and N. Sutin. *Biochim. Biophys. Acta*, 811:265, 1985.
- [36] H. Bässler. *Phys. Stat. Sol. B*, 175:15, 1993.
- [37] F. Flores and C. Tejedor. *J. Phys. C: Solid State Physics.*, 20:145, 1987.
- [38] G. Margaritondo and F. Capasso. *Heterojunction Band Discontinuities - Physics and Device Applications, Chapter 1 : The theory of heterojunction band lineups*. North Holland, Amsterdam, 1987.
- [39] W. Monch. *Festkörperprobleme*, XXVI:67, 1986.
- [40] H. Luth. *Springer Series in Surface Sciences 15; Vol. 15*. Springer, Berlin, 1993.

- [41] G. Margaritondo. *Electronic Structure of Semiconductor Heterojunctions*. Jaca Book, Milano, 1988.
- [42] J. Tersoff. *Phys. Rev. B*, 30:4874, 1984.
- [43] J. Tersoff. *Phys. Rev. B*, 32:6968, 1985.
- [44] H. Vázquez, F. Flores, and A. Kahn. *Proc. Int. Symp. Super-Functionality Organic Devices*, 6:1, 2005.
- [45] S. Kurtin, T. C. McGill, and C. A. Mead. *Phys. Rev. Lett.*, 22:1433, 1969.
- [46] M. Schluter. *Phys. Rev. B*, 17:5044, 1978.
- [47] L. Magaud and F. Cyrot-Lackmann. *Encyclopedia of Applied Physics; Vol. 16, p. 573-591*. VCH Publishers, New York, 1996.
- [48] H. Ishii, K. Sugiyama, E. Ito, and K. Seki. *Adv. Mater.*, 11:605, 1999.
- [49] I. G. Hill, A. Rajagopal, A. Kahn, and Y. Hu. *Appl. Phys. Lett.*, 73:662, 1998.
- [50] Y. Park, V. Choong, and Y. Gao. *Appl. Phys. Lett.*, 69:1080, 1996.
- [51] I. H. Campbell, J. D. Kress, R. L. Martin, D. L. Smith, N. N. Barashkov, and J. P. Ferraris. *Appl. Phys. Lett.*, 71:3528, 1997.
- [52] Kwanghee Lee, Jon Young Kim, Sung Heum Park, Sun Hee Kim, Shinuk Cho, and Alan J. Heeger. *Adv. Mater.*, 19:2445, 2007.
- [53] R. D. Scurlock, B. Wang, P. R. Ogilby, J. R. Sheats, and L. Clough. *J. Am. Chem. Soc.*, 117:10194, 1995.
- [54] K. Z. Xing, N. Johansson, G. Beamson, D. T. Clark, J. L. Bredas, and W. R. Salaneck. *Adv. Mater.*, 9:1027, 1997.
- [55] A. P. Monkman, H. D. Burrows, M. da G. Miguel, I. Hamblett, and S. Navaratnam. *Chem. Phys. Lett.*, 307:303, 1999.
- [56] A. Fujishima and K. Honda. *Nature*, 238:37, 1972.

- [57] A. L. Linsebigler, G. Lu, and J. T. Yates Jr. *Chem. Rev.*, 95:735, 1995.
- [58] V. E. Henrich and P. A. Cox. *The Surface Science of Metal Oxides, Chapter 7 : Interfaces of metal oxides with metals and other oxides*. Cambridge University Press, Cambridge, 1994.
- [59] C. Noguera. *Physics and Chemistry of Oxide Surfaces, Chapter 4 : Metal oxide Interfaces*. Cambridge University Press, Cambridge, 1996.
- [60] H. J. Bolink, E. Coronado, D. Repetto, and M. Sessolo. *Applied Physics Letters*, 91:223501, 2007.
- [61] C. W. Chen, Y. J. Lu, C. C. Wu, E. H. E. Wu, C. W. Chi, and Y. Yang. *Appl. Phys. Lett.*, 87:241121, 2005.
- [62] N. Tokmoldin, N. Griffiths, D. D. C. Bradley, and S. A. Haque. *Adv. Mat.*, 21:3475, 2009.
- [63] D. Kabra, M. H. Song, B. Wenger, R. H. Friend, and H. J. Snaith. *Advanced Materials*, 20:3447, 2008.
- [64] M. H. Ho, S. F. Hsu, J. W. Ma, S. W. Hwang, P. C. Yeh, and C. H. Chen. *Appl. Phys. Lett.*, 91:113518, 2007.
- [65] S. H. Kim, J. Y. Kim, S. H. Park, and K. Lee. *Proc. SPIE-Int. Soc. Opt. Eng.*, page 5937, 2005.
- [66] Z. L. Wang, X.Y. Kong, Y. Ding, P. Gao, L. Hughes, R. Yand, and Y. Zhang. *Adv. Funct. Mater.*, 14:943, 2004.
- [67] C. Ye, X. Fang, Y. Hao, X. Teng, and L. Zhang. *J. Phys. Chem. B*, 109:19758, 2005.
- [68] M. Cardona. *Modulation Spectroscopy*. Academic, New York, 1969.
- [69] Edited by T. S. Moss D. E. Aspnes and M. Balkanski. *Handbook on Semiconductors; Vol. 2, p. 109-154*. North-Holland, Amsterdam, 1981.

- [70] G. Weiser. *Phys. Stat. Sol.*, 18:347, 1973.
- [71] S. D. Philips, R. Worland, G. Yu, T. Hagler, R. Freedman, Y. Cao, V. Yoon, J. Chiang, W. C. Walker, and A. J. Heeger. *Phys. Rev. B*, 40:9751, 1989.
- [72] P. Butcher and D. Cotter. *The Elements of Nonlinear Optics*. Cambridge University Press, Cambridge, 1990.
- [73] W. D. Bruce and D. O'Hare. *Inorganic Materials*. Wiley, Chichester, 1992.
- [74] P. N. Prasad and D. J. Williams. *Introduction to Nonlinear Optical Effects in Molecules and Polymers*. John Wiley and Sons, New York, 1991.
- [75] H. Uchiki and T. Kobayashi. *J. Appl. Phys.*, 64:2625, 1988.
- [76] B. H. Bransden and C. J. Joachain. *Physics of Atoms and Molecules*. Longman Scientific and Technical, New York, 1983.
- [77] A. Horvath, G. Weiser, G. L. Baker, and S. Etemad. *Phys. Rev. B*, 51:2751, 1995.
- [78] G. Weiser and A. Horvath. *Chem. Phys.*, 227:153, 1998.
- [79] A. Horvath, H. Bässler, and G. Weiser. *Phys. Stat. Sol.*, 173:755, 1992.
- [80] L. Sebastian, G. Weiser, and H. Bässler. *Chem. Phys.*, 61:125, 1981.
- [81] P. S. Davids, A. Saxena, D. L. Smith, and J. L. Smith. *J. Appl. Phys.*, 78:4244, 1995.
- [82] I. H. Campbell, D. L. Smith, and J. P. Ferraris. *Appl. Phys. Lett.*, 66:3030, 1995.
- [83] J. R. Lakowicz. *Principles of fluorescence spectroscopy, second edition, Chapter 4 : Time-domain Lifetime Measurements*. Kluwer Academic/Plenum Publishers, New York, 1999.

- [84] D. V. O'Connor and D. Philips. *Time-Correlated Single Photon Counting, Chapter 2 : Basic Principles of the Single Photon Counting Lifetime Measurements*. Academic Press, New York, 1984.
- [85] M. G. Badea and L. Brand. *Methods in Enzymol*, 61:378, 1971.
- [86] D. E. Markov and P. W. M. Blom. *Phys. Rev. B*, 72:161401, 2005.
- [87] H. Becker, S. E. Burns, and R. H. Friend. *Phys. Rev. B*, 56(4):1893–1905, Jul 1997.
- [88] M. N. Bussac, D. Michoud, and L. Zuppiroli. *Phys. Rev. Lett.*, 81:1678, 1998.
- [89] P. Bröms, J. Birgersson, N. Johansson, M. Lögdlund, and W. R. Salaneck. *Synthetic metals*, 74:179, 1995.
- [90] J. M. Bharanthan and Y. Yang. *Journ. Appl. Phys.*, 84:3207, 1998.
- [91] M. K. Fung, L. L. Lai, S. W. Tong, C. S. Lee, and S. T. Lee. *Journ. Appl. Phys.*, 94:5763, 2003.
- [92] H. Bäessler, V. I. Arkhipov, E. V. Emelianova, A. Gerhard, A. Haver, C. Im, and J. Rissler. *Synthetic Metals*, 135-136:377, 2003.
- [93] K. Morii, M. Omoto, M. Ishida, and M. Graetzel. *Japanese Journal of Applied Physics*, 47:7366, 2008.
- [94] J. S. Kim, R. H. Friend, I. Grizzi, and J. H. Burroughes. *Applied Physics Letters*, 87:023506, 2005.
- [95] M. A. Stevens, C. Silva, D. M. Russell, and R. H. Friend. *Phys. Rev. B.*, 63:165213, 2001.
- [96] H. Kuhn. *Jour. Chem. Phys.*, 53:101, 1970.
- [97] R. R. Chance, A. Prock, and R. Silbey. *Jour. Chem. Phys.*, 62:2245, 1975.
- [98] T. Förster. *Modern Quantum Theory, Vol. III*. Academic, New York, 1965.

- [99] C. M. Ramsdale and N. C. Greenham. *J. Phys. D: Appl. Phys.*, 36:L29, 2003.
- [100] M. Al-Kuhaili, S. Durrani, I. Bakhtiari, and A. Al-Shurkri. *Optics communications*, 283:2857, 2010.
- [101] Zahid Hussain. *Journal of Applied Physics*, 91:5745, 2002.
- [102] T. S. Sian and G. Reddy. *Jour. of Sol. Mat.*, 82:375, 2004.
- [103] E. A. Stern and R. A. Ferrell. *Phys. Rev.*, 120:130, 1960.
- [104] S. A. Jenekhe and J. A. Osaheni. *Science*, 265:765, 1994.
- [105] A. C. Morteani, A. S. Dhoot, J. S. Kim, C. Silva, N. C. Greenham, C. Murphy, E. Moons, S. Cina, J. H. Burroughes, and R. H. Friend. *Adv. Mater.*, 20:1708, 2003.
- [106] A. C. Morteani, P. Sreearunothai, L. M. Herz, R. H. Friend, and C. Silva. *Phys. Rev. Lett.*, 92:247402, 2004.
- [107] Y. S. Huang, S. Westenhoff, I. Avilov, P. Sreearunothai, J. M. Hodgkiss, C. Deleener, R. H. Friend, and D. Beljonne. *Nature Mat.*, 7:483, 2008.
- [108] T. Matsushima, Y. Kinoshita, and H. Murata. *Applied Physics Letters*, 91:253504, 2007.
- [109] L. Cattin, F. Dahou, Y. Lare, M. Morsli, R. Tricot, S. Houari, A. Mokrani, K. Jondo, A. Khelil, K. Napo, and J. C. Bernede. *Applied Physics Letters*, 105:034507, 2009.
- [110] M. Kroger, S. Hamwi, J. Meyer, T. Riedl, W. Kowalsky, and A. Kahn. *Applied Physics Letters*, 95:123301, 2009.
- [111] M. Kröger, S. Hamwi, J. Meer, T. Riedl, W. Kowalsky, and A. Kahn. *Organic Electronics*, 10:932, 2009.
- [112] Y. Kinoshita, R. Takenaka, and H. Murata. *Applied Physics Letters*, 92:243309, 2008.

- [113] W. Y. Jiang, Z. L. Zhang, J. Cao, M. A. Khan, K.U. Haq, and W. Q. Zhu. *Journal of Physics D: Applied Physics*, 40:5553, 2007.
- [114] S. K. Deb and J. A. Chopoorian. *Journal of Applied Physics*, 37:4818–4825, 1966.
- [115] S. K. Deb. *Proc. Roy. Soc. A*, 304:211, 1968.
- [116] B. W. Faughnan, R. S. Crandall, and P. M. Heyman. *RCA REVIEW*, 36:177–197, 1975.
- [117] O. F. Schirmer, V. Wittwer, G. Baur, and G. Brandt. *J. Electrochem. Soc.*, 124:749–753, 1977.
- [118] T. He and J. Yao. *Journal of Photochemistry and Photobiology*, 4:125, 2003.
- [119] T. M. Brown, J. S. Kim, R. H. Friend, and F. Cacialli. *Applied Physics Letters*, 75:1679, 1999.
- [120] G. Winroth, G. Latini, D. Credginton, L. Wong, L. Chua, P. J. Ho, and F. Cacialli. *Applied Physics Letters*, 92:103308, 2008.
- [121] J. S. Kim, B. Lägél, E. Moons, N. Johansson, I. D. Baikie, W. R. Salaneck, R. H. Friend, and F. Cacialli. *Synthetic Metals*, 2000:311, 2000.
- [122] M. Pal, Y. Tsugami, K. Hirota, and H. Sakata. *J. Phys. D: Appl. Phys.*, 34:459, 2001.
- [123] M. S. Whittingham. *Solid State Ionics*, 168:255, 2004.
- [124] N. F. Mott. *Metal-Insulator Transitions, Second Edition, Chapter 7 : Metal-insulator transitions in transitional-metal oxides*. Taylor and Francis, London, UK, 1990.
- [125] V. R. Porter, W. B. White, and R. Roy. *Solid State Chem.*, 4:250–254, 1972.
- [126] M. Dieterle, G. Weinberg, and G. Mestl. *Phys. Chem. Chem. Phys.*, 4:812–821, 2002.

- [127] G. J. Exarhos and X. D. Zhou. *Thin Solid Films*, 515:7025, 2007.
- [128] X. Deng, S. Y. Quek, M. M. Biener, J. Bienr, D. H. Kang, R. Schalek, E. Kaxiras, and C. M. Friend. *Surface Science*, 602:1166, 2008.
- [129] J. Meyer, A. Shu, M. Kröger, and A. Kahn. *Applied Physics Letters*, 96:133308, 2010.
- [130] M. Zhang, Irfan, H. Ding, Y. Gao, and C. W. Tang. *Applied Physics Letters*, 96:183301, 2010.
- [131] Irfan, H. Ding, Y. Gao, C. Small, D. Y. Kim, J. Shubbiah, and F. So. *Applied Physics Letters*, 96:243307, 2010.
- [132] E. Moons. *J. Phys.: Condens. Matter*, 14:12235–12260, 2002.
- [133] K. Jacobi, G. Zwicker, and A. Gutmann. *Surface Science*, 141:109, 1984.
- [134] H. Moormann, D. Kohl, and G. Heiland. *Surface Science*, 100:302, 1980.